International Journal of
Molecular Sciences

MDPI

Article

Novel Pyridine-Based Thiazolyl-Hydrazone as a Promising Attenuator of *Pseudomonas aeruginosa* Pathogenicity by Targeting Quorum Sensing

Anabela Borges [1,2,*,†], Sanja Kokanov [3,†], Miguel M. Leitão [1,4], Predrag Ristić [3], Irena Novaković [5], Vladimir Dobričić [6], Milan Nikolić [3], Mire Zloh [7,8], Tamara R. Todorović [3], Manuel Simões [1,2] and Nenad R. Filipović [9,*]

1 LEPABE (Laboratory for Process Engineering, Environment, Biotechnology and Energy, Faculty of Engineering), ALiCE (Associate Laboratory for Innovation in Chemical Engineering), Faculty of Engineering, University of Porto, Rua Dr. Roberto Frias, 4200-465 Porto, Portugal; up202111359@edu.fe.up.pt (M.M.L.); mvs@fe.up.pt (M.S.)
2 DEQB—Department of Chemical and Biological Engineering, Faculty of Engineering, University of Porto, Rua Dr. Roberto Frias, s/n, 4200-465 Porto, Portugal
3 Faculty of Chemistry, University of Belgrade, Studentski trg 12-16, 11000 Belgrade, Serbia; markovics@chem.bg.ac.rs (S.K.); predrag@chem.bg.ac.rs (P.R.); mnikolic@chem.bg.ac.rs (M.N.); tamarat@chem.bg.ac.rs (T.R.T.)
4 MedInUP, Center for Drug Discovery and Innovative Medicines, University of Porto, 4200-319 Porto, Portugal
5 Institute of Chemistry, Technology and Metallurgy, University of Belgrade, Njegoševa 12, 11000 Belgrade, Serbia; irena.novakovic@ihtm.bg.ac.rs
6 Department of Pharmaceutical Chemistry, Faculty of Pharmacy, University of Belgrade, Vojvode Stepe 450, 11221 Belgrade, Serbia; vladimir@pharmacy.bg.ac.rs
7 UCL School of Pharmacy, University College London, 29/39 Brunswick Square, London WC1N 1AX, UK; mire.zloh@ffns.ac.rs
8 Faculty of Pharmacy Novi Sad, University Business Academy in Novi Sad, Heroja Pinkija 4, 21101 Novi Sad, Serbia
9 Faculty of Agriculture, University of Belgrade, Nemanjina 6, 11000 Belgrade, Serbia
* Correspondence: apborges@fe.up.pt (A.B.); nenadf@agrif.bg.ac.rs (N.R.F.); Tel.: +351-22041-4968 (A.B.); +381-11441-3148 (N.R.F.)
† These authors contributed equally to this manuscript.

Abstract

Pseudomonas aeruginosa biofilm-associated infections present higher recalcitrance to antimicrobial treatments, contributing to persistent and difficult-to-treat infections. Quorum sensing (QS) regulates various cellular processes that are important for the establishment and survival of microbial communities on the host. However, QS inhibitors for the treatment of *P. aeruginosa* biofilms remain under-researched, partly due to the complexity of QS signalling pathways and the challenge of developing non-toxic inhibitors. Herein, the bioactivity of 2-{(2*E*)-2-[1-(pyridin-2-yl)ethylidene]hydrazinyl}-1,3-thiazole-4-carboxylic acid (**TTNF37**), a novel pyridine-based thiazolyl-hydrazone (PTH), was investigated. The compound antimicrobial activity was evaluated against a broad spectrum of microorganisms, its antioxidant potential was assessed using different assays, and its QS-inhibitory effect on *P. aeruginosa* was studied using bioreporter strains. The effect on *P. aeruginosa* biofilm formation was analysed in terms of biomass, culturability, and metabolic activity, structure, and cell membrane integrity, while virulence factors were evaluated through absorbance measurements. In addition, molecular docking studies were performed to predict the drug's interactions with essential QS proteins and biological targets. **TTNF37** exhibited potent antimicrobial activity with low to moderate minimum inhibitory concentrations against clinically relevant Gram-negative and Gram-positive bacteria, as well as fungi and yeasts. It also showed antioxidant activity, with variable effectiveness across different radicals and systems. **TTNF37** inhibited the 3-oxo-C12-HSL-dependent QS system

Check for updates

Academic Editor: Antonella Piozzi

Received: 22 December 2025
Revised: 30 January 2026
Accepted: 5 February 2026
Published: 12 February 2026

Copyright: © 2026 by the authors. Licensee MDPI, Basel, Switzerland. This article is an open access article distributed under the terms and conditions of the Creative Commons Attribution (CC BY) license.

of *P. aeruginosa* in a dose-dependent manner, with reductions ranging from 26% to 98%. It also impaired the production and detection of 3-oxo-C12-HSL, resulting in a 56% and 65% decrease in bioluminescence, respectively. Molecular docking studies revealed strong binding interactions with LasI and LasR proteins, with affinity values exceeding those of furvina, a known potent QS inhibitor. Molecular dynamics simulations validated stable **TTNF37** binding to LasR and LasI. Both experimental and docking data indicate a significant interaction with human serum albumin (HSA). **TTNF37** also significantly reduced pyocyanin production and prevented biofilm set-up with a reduction of 50% in biomass with pronounced alterations in biofilm structure. These results indicate the potential of **TTNF37** and related PTHs for treating biofilm-associated infections.

Keywords: antibacterial resistance; biofilm prevention; quorum-sensing inhibition; *Pseudomonas aeruginosa*; molecular dynamics; docking

1. Introduction

Resistance to antibiotics, especially when a biofilm has formed, is a major problem in the treatment of bacterial infections [1,2]. Biofilms allow bacteria to acquire high tolerance and/or resistance (recalcitrance) to antibacterial agents and host immunity [2,3]. To date, there are no effective therapies for the treatment of infections associated with biofilms, which lead to chronicity and increased patient morbidity and mortality [4]. The high virulence and pathogenicity of bacterial biofilm are closely linked to their ability to form organized communities and modulate gene expression during biofilm lifestyle, exhibiting behavior that is distinctly different from that of their planktonic state. This regulation occurs through cell-to-cell communication, a process known as quorum sensing (QS) [5].

Bacteria use this signaling system to regulate various collective behaviors (e.g., bioluminescence, competence, conjugation, sporulation, symbiosis, motility, secretion of toxins, virulence factors, and antimicrobial compounds, production of public goods, and biofilm formation/differentiation). Extracellular self-generated signaling molecules, called autoinducers (AIs), mediate this intercellular communication system. When the concentration of AIs attains the "quorum" level, the bacteria can alter the global gene expression patterns [1,2,6]. The expression of QS-regulated genes can affect the behaviour of the bacteria and the host's response during infection (i.e., immunomodulation) [7,8]. Indeed, it has been found that different types of autoinducers (e.g., homoserine lactones (HSL), quinolones, and phenazines) are crucial for bacterial interaction with the host cells and, thus, colonization [9].

Pseudomonas aeruginosa is widely recognized for its ability to form biofilms on medical devices and human tissue, contributing to persistent and difficult-to-treat infections. These biofilms play a key role in the pathogen's recalcitrance to antibiotics and its involvement in chronic diseases, including cystic fibrosis, lung infections, pneumonia, and endocarditis [4,10]. This bacterium depends on QS to control the biofilm formation as well as the synthesis of several virulence factors, including proteases, exotoxin A, siderophores (pyoverdine and pyochelin), and pyocyanin, which contribute to tissue damage, immune evasion, and antibiotic resistance [11]. The expression of these virulence factors in *P. aeruginosa* occurs via four hierarchically organized QS systems called las, rhl, pqs, and Iqs. The most important is the las (LasI/R) system, as it is at the top of the chain and thus has a direct influence on the other three systems [12,13]. In particular, this system is composed of LasI, which controls the synthesis of N-(3-oxo-dodecanoyl)-HSL (3-oxo-C12-HSL), which in turn binds and activates the LasR regulator protein.

QS inhibitors (QSIs) are compounds that can interfere with the QS system, thereby affecting bacterial pathogenicity and virulence. They can act at the level of AIs synthesis and recognition by competitively binding or structurally altering the AIs synthesis or receptor proteins. In addition, QSIs can lead to the enzymatic degradation of AIs or their elimination by antibodies or macromolecules (e.g., cyclodextrins) [4,14]. Due to the differential mode of actuation, QSIs could enable the reduction in bacterial adaptability, intense selective pressure by antibiotics use, and biofilm formation/differentiation, representing a promising alternative to current antimicrobial agents. However, none of the QSIs identified to date have found clinical application, mainly due to their poor bioavailability and toxicity. In addition, the production yield of natural QSIs is generally low [14,15]. In that way, a hopeful approach to overcome these limitations is the rational design of new inhibitors.

Modern drug design is still based on a pharmacophore hybridisation strategy. In recent years, novel compounds exhibiting promising antimicrobial activity have been designed using this approach [16–20]. A recently published survey of the U.S. FDA-approved drugs reveals that the number of drugs based on heterocyclic pharmacophores is increasing. Namely, in the 11-year period (2013–2023), 82% of the small molecules approved as drugs contain at least one heterocycle. Among these drugs, the pyridine pharmacophore is the most frequently occurring in the mentioned dataset of compounds [21]. In this regard, the FDA has recently approved nine pyridine-based compounds as antibiotics for the treatment of human infections (Table 1). Moreover, numerous novel pyridine-based compounds have been reported as potent antimicrobial agents [22,23].

Table 1. Antimicrobial drugs based on pyridine, thiazole, and hydrazone pharmacophores approved by the FDA [24,25].

Pharmacophore	Antimicrobial Drugs
Pyridine	Otesecinazole, Tedizolid phosphate, Isavucunazonium, Izoniazid, Ibrexafungerp citrate, Cefatizidime, Delafloxacin, Ozenoxacin, and Isavuconazonium (antifungal)
Thiazole	Cefepime, Aztreonam, Cefixime, Ceftazidime, Ceftriaxone, Cefotaxime, Cefpodoxime, Nitazoxanide, Cefdinir, Ceftaroline fosamil, Cobicistat, Isavuconazonium, and Cefiderocol
Hydrazone	Furagin (Furazidine), Rifapentine, Rifampicin, Nifurtimox (antiparasitic)

The thiazole heterocycle is another frequently used heterocyclic pharmacophore in the design of small-molecule drugs [21]. Currently, 27 thiazole-based drugs are approved by the U.S. FDA. Among them, the majority (13) are approved for the treatment of diseases caused by microbes (Table 1). Many of the new thiazole-based small molecules have recently been shown to be promising antimicrobial agents [26].

The hydrazone moiety serves as a linker to bridge two pharmacophores, thereby forming molecular hybrids [27–29], and is also considered an important pharmacophore in medicinal chemistry [27]. Hydrazones exhibit a broad spectrum of biological activities, including antimicrobial activity. Currently, four antimicrobial drugs based on a hydrazone moiety have been approved by the U.S. FDA for the treatment of human infections (Table 1).

Molecular hybrids in which a hydrazone moiety bridges pyridine and thiazole pharmacophores are called pyridine-based thiazolyl hydrazones (PTHs). PTHs are known to inhibit various enzymes with respective roles in diabetes, neurodegeneration, and cancer. These compounds also exhibit various kinds of biological activities, including antimicrobial activity [28]. In our previous study, we tested the antibacterial activity of several PTHs,

including (*E*)-2-(2-(pyridin-2-ylmethylene)hydrazinyl)-4-(*p*-tolyl)thiazole (HL; Figure 1), as well as their Co(III) complexes, against several bacteria using the disc-diffusion method. This method was chosen because of the low solubility of the PTH ligands. The results indicated that all ligands were inactive, while corresponding complexes showed appreciable activity [29]. In our further study, mechanistic investigations of $Co(HL)_2$, Co(III) complex with HL, revealed that its antimicrobial activity against *Pseudomonas aeruginosa* is related to its ability to inhibit the 3-oxo-C12-HSL-dependent quorum-sensing system [11]. Docking studies indicated that $Co(HL)_2$ itself is not an inhibitor of the transcriptional activator protein LasR, but rather serves as a delivery system for HL, which forms the strongest interactions compared to both furvina and the co-crystallized ligand 3-oxo-C12-HSL. To obtain a soluble HL derivative that can also act as the *P. aeruginosa* inhibitor of LasR, we designed a novel molecule (**1**) by the replacement of a hydrophobic tolyl group with a hydrophilic carboxyl group (Figure 1). After testing its activity against *P. aeruginosa*, the obtained MIC value was not small enough to consider **1** as a potent inhibitor of LasR [30]. Because of that, we introduced a small structural change to enhance its hydrophobicity by replacing the hydrogen atom from the periphery of ligand **1** with a methyl group, resulting in the novel compound, **TTNF37** (Figure 1), which is the subject of the current investigation.

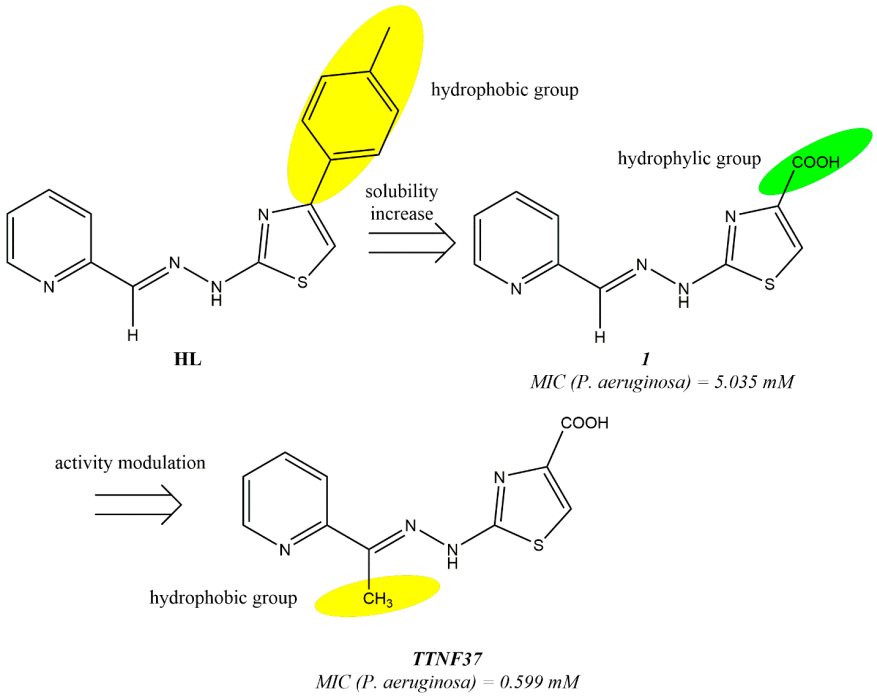


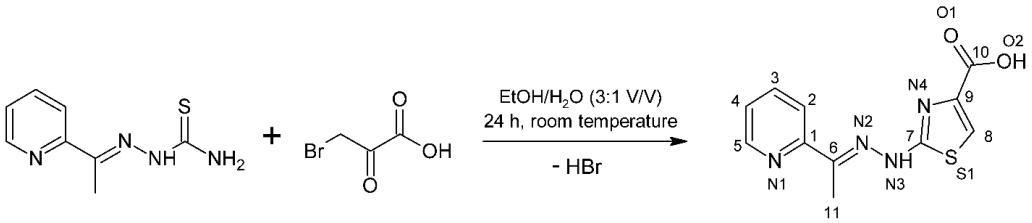
Figure 1. Design strategy of **TTNF37**.

In this work, the antimicrobial activity of **TTNF37** against a panel of clinically relevant Gram-negative (*Escherichia coli*, *Pseudomonas aeruginosa*, *Proteus hauseri*, *Klebsiella pneumoniae*, *Salmonella enterica* subsp. *enterica* serovar *Enteritidis*) and Gram-positive (*Staphylococcus aureus*, *Clostridium sporogenes*, *Micrococcus luteus*, *Bacillus subtilis*) bacteria, as well as yeast (*Candida albicans*, *Saccharomyces cerevisiae*) and fungi (*Aspergillus brasilliensis*), was first evaluated, followed by the assessment of its antioxidant potential as well as antiproliferative activity against MRC-5 (Medical Research Council cell strain 5) normal cell line. Then, **TTNF37** was investigated for its ability to disrupt the LasI/R QS system of *P. aeruginosa* (in silico and in vitro) and to inhibit QS-regulated phenotypes—the production of virulent factors (pioverdin and piocyanin) and biofilm formation. Lastly, given the importance of Human serum albumin (HSA) for the delivery of antibiotics through the bloodstream [31], interactions between **TTNF37** and this protein were also studied experimentally and in silico.

2. Results and Discussion

2.1. Synthesis and Characterization

TTNF37 was prepared by the Hantzsch reaction between 2-acetylpiridine thiosemicarbazone and bromopyruvic acid (Scheme 1). Since HBr is the by-product of this reaction, it is possible to obtain TH-hydrobromide salt. In our previous study, we demonstrated that TH-hydrobromide salts can be obtained when the Hantzsch reaction is performed in ethanol. At the same time, hydrobromide formation can be prevented if the solvent is a mixture of water and ethanol. Such reaction conditions imply that water acts as a base [29]. Because of that, **TTNF37** was prepared by the addition of solid bromopyruvic acid into the suspension of 2-acetylpiridine thiosemicarbazone into the mixture of EtOH/H_2O (1:3). Obtained ocher powder was filtered and washed with cold water, EtOH, and Et_2O, and purified by vapor diffusion of EtOH into dimethyl sulphoxide (DMSO) solution of the crude product.



Scheme 1. Synthetic procedure for **TTNF37**.

The composition of **TTNF37** was confirmed by elemental analysis, while its structure was validated by spectroscopic methods (FTIR and NMR spectroscopy). In the FTIR spectrum (Figure S1A), a characteristic broadening is observed from 3400 to 3000 cm^{-1}, representing the region of hydrogen bonding and stretching O–H and N–H vibrations. At 1718 cm^{-1}, a strong band characteristic of the stretching vibration of the C=O bond was identified. A very strong band, originating from the C=N stretching vibration, was observed at 1577 cm^{-1}. C–S stretching vibrations of the thiazole ring were observed in the region of 853–800 cm^{-1}. Also, in the absorption region of 779 to 493 cm^{-1}, ring vibrations were observed [32,33]. The overlaid FTIR spectra of **TTNF37** and the corresponding reactants, clearly illustrating the associated spectral changes (Figure S1B).

Since the imine bond can adopt either an *E* or *Z* configuration, **TTNF37** can be found in one of these configurations or exist simultaneously as a mixture of *E*/*Z* isomers. The ^1H and ^{13}C NMR spectra clearly show the existence of a single set of signals, indicating the presence of a single configurational isomer (Figures S2 and S3).

Based on the chemical shift in the N3–H proton (12.16 ppm), it was concluded that the *E*-isomeric form of **TTNF37** is present in the solution. Additionally, the existence of the *Z*-isomer implies the presence of an intramolecular hydrogen interaction between the hydrazone N–H hydrogen atom and the pyridine nitrogen atom. This is not the case, since the chemical shift in the N–NH hydrogen would be significantly shifted towards the lower field (~2–3 ppm) [34,35].

A singlet originating from the methyl group was observed at 2.36 ppm. Aromatic protons are in the range of 7.32–8.55 ppm, while at 12.16 ppm, a characteristic extended singlet originating from hydrazone N–H and carboxylic O–H protons was observed (Table 2). Assignment of ^1H and ^{13}C signals in the structure of **TTNF37** in a DMSO-d_6 solution was performed by analyzing 2D NMR spectra (COSY, HSQC, and HMBC, Figures S4–S6, respectively).

Table 2. Assignment of ^{1}H and ^{13}C signals in **TTNF37**.

1H-NMR	13C-NMR
δ: 2.36 (s, 3H, H11–C11); 7.34 (dd, 1H, H–C4); 7.72 (s, 1H, H–C8); 7.81 (td, 1H, H–C3); 7.98 (d, 1H, H–C2); 8.55 (s, 1H, H–C5); 12.16 (s, 2H, N3–H, O2–H).	δ: 12.74 (C11); 119.60 (C8); 120.00 (C2); 123.94 (C4); 137.00 (C3); 144.37 (C9); 147.89 (C6); 149.04 (C5); 155.20 (C1); 162.84 (C10); 169.51 (C7).

2.2. Bioactivity

2.2.1. Antimicrobial Profile

To verify the antimicrobial activity of **TTNF37**, its minimum inhibitory concentration (MIC) against a panel of clinically relevant Gram-negative and Gram-positive bacteria, as well as fungi, was initially determined. Erythromycin and amphotericin B (broad-spectrum antibiotic/antifungal) were positive controls for bacteria and fungi, respectively [36]. In general, from the preliminary screening of their antimicrobial activity, it was observed that **TTNF37** acted as a moderate antibacterial agent with MIC values in the range of 39.1–314.0 μg/mL for bacteria and a weak antifungal agent with MIC values in the range of 1250.0–2499.9 μg/mL for fungi (Table 3). It is noteworthy that for *E. coli*, the MIC value (39.1 μg/mL) was very close to that obtained for the antibiotic erythromycin (27.9 μg/mL). However, the MIC values obtained against the studied fungi were significantly higher, in some cases over 100-fold (*C. albicans* = 2499.9 μg/mL; *S. cerevisiae* = 1250.0 μg/mL) compared to the antifungal agent amphotericin B (*C. albicans* = 20.33 μg/mL; *S. cerevisiae* = 10.16 μg/mL). The results presented are consistent with those obtained by Kassab et al. [37] with synthesised thiazole derivatives 14a–e. The authors observed that against *E. coli* ATCC 25922, isatin-decorated thiazole derivatives had MICs of 4 μg/mL for the best compounds and 256 μg/mL for the worst. For MRSA ATCC 43300, the best compound had an MIC of 32 μg/mL, while the worst was 256 μg/mL. In the present study, the **TTNF37** showed MIC values comparable to the most effective compounds described previously, except in the case of *C. albicans*, where a much higher MIC was observed.

Table 3. MIC values (μg/mL) of **TTNF37** and reference antimicrobials (antibiotic and antifungal agents) against selected microorganisms.

	MIC (μg/mL)												
Compounds	*E. coli*	*P. aerugi-nosa*	*P. hauseri*	*K. pneu-moniae*	*S. enterica*	*S. aureus*	*M. luteus* (ATCC 4698)	*M. luteus* (ATCC 10240)	*B. subtilis*	*C. sporo-genes*	*C. albicans*	*A. brazilien-sis*	*S. cerevisiae*
TTNF37	39.1	157.1	157.1	157.1	157.1	157.1	78.4	314.0	78.4	314.0	2499.9	1250.0	1250.0
Erythromycin	27.9	55.8	27.9	27.9	27.9	55.8	13.9	27.9	55.8	55.8	n.d.	n.d.	n.d.
Amphotericin B	n.d.	n.d.	n.d.	n.d.	n.d.	n.d.	n.d.	n.d.	n.d.	n.d.	20.33	40.66	10.16

n.d: Not determined.

2.2.2. Antioxidant Profile

By modulating oxidative stress, compounds with antioxidant properties may support the overall management and recovery from microbial infections [38,39]. Although reactive oxygen species (ROS) are associated with oxidative stress and can lead to cell wall destruction and bacterial death, pro-oxidant compounds can paradoxically favour bacterial biofilm infections. This occurs because some bacteria can use ROS as signal molecules to activate genes associated with QS, inducing biofilm formation [40]. In particular, Wei et al. [41] demonstrated that exposure of *P. aeruginosa* to hydrogen peroxide activates the OxyR regulator, which causes the expression of antioxidant genes (*katA*, *katB*, *ahpB*, and *ahpCF*). However, the authors found that this regulator was also involved in the regulation

of genes related to biofilm formation (*pf4* and *bdlA*), QS (*rsaL*), and many other processes (iron homeostasis (pvdS), protein synthesis (rpsL), and oxidative phosphorylation (*cyoA* and *snr1*)). This shows that ROS not only exerts a cytotoxic effect but also acts as a signal for bacterial adaptation and biofilm formation.

In that way, in this study, a comprehensive evaluation of the antioxidant potential of **TTNF37** was conducted. For this, a combination of different methods was used and included ABTS (2,2′-azino-bis(3-ethylbenzothiazoline-6-sulfonic acid)), DPPH (2,2-diphenyl-1-picrylhydrazyl), TAOC (Total Antioxidant Capacity), •NO (Nitric oxide), ORAC (Oxygen Radical Absorbance Capacity), and HORAC (Hydroxyl Radical Antioxidant Capacity) assays. Vitamin C was chosen for its known antioxidant potential and is a widely used standard, as it acts primarily as a donor of a single hydrogen atom. Furthermore, the resulting monodehydroascorbate radical anion primarily reacts with radicals, thereby further contributing to its antioxidant properties [42]. From the data obtained in the evaluation of the antioxidant capacity of **TTNF37** (Table 4), it appears that the compound exhibits antioxidant activity, albeit with varying efficacy, depending on the specific radical or system used in the assay. Overall, **TTNF37** showed lower antioxidant activity than vitamin C in most of the assays tested. In the ABTS (51.7 µg/mL) and DPPH (144.3 µg/mL) assays, **TTNF37** displayed higher IC_{50} values than vitamin C (ABTS = 40.85 µg/mL and DPPH = 46.85 µg/mL), indicating lower radical-scavenging efficiency. A similar trend was observed in the TAOC assay, where **TTNF37** (262.6 µg/mL) required substantially higher concentrations than vitamin C (42.27 µg/mL) to achieve comparable antioxidant effects, further confirming its reduced efficiency. In contrast, **TTNF37** (136.4 µg/mL) showed comparable antioxidant performance to vitamin C (124.95 µg/mL) in the •NO assay, with IC_{50} values of the same order of magnitude. Notably, the most favourable result for **TTNF37** (160.8 µg/mL) was observed in the ORAC and HORAC assays, where its activity was similar to, or slightly higher than, that of vitamin C (155.7 µg/mL), suggesting a more effective scavenging capacity against radicals under these conditions.

Table 4. Antioxidant activity values of **TTNF37** measured by ABTS, DPPH, TAOC, •NO, ORAC, and HORAC methods.

	Antioxidant Activity					
Compounds	**ABTS: IC_{50} (µg/mL)**	**DPPH: IC_{50} (µg/mL)**	**TAOC: EC_{50} (µg/mL)**	**•NO: IC_{50} (µg/mL)**	**ORAC (µg/mL)**	**HORAC (µg/mL)**
TTNF37	51.7	144.3	262.6	136.4	160.8	134.3
Vitamin C	40.85	46.85	42.27	124.95	155.7	160.4

The antioxidant effect of **TTNF37** can be explained by analyzing the role of the hydrazone and thiazole groups. The hydrazone double bond enables electrons to move between the two neighboring aromatic rings of the compound, resulting in different resonance structures [43]. As a result, the hydrazone group acts as an electron donor, helping to eliminate free radicals. In addition, the ease with which the NH proton is released makes compounds with the hydrazone group potent free radical scavengers [44]. Regarding the thiazole group, the results are consistent with those of a study performed by Jaishree et al. [45], who found that thiazole derivatives exhibit better antioxidant properties than vitamin C, as evidenced by their ability to inhibit nitric oxide radicals, hydrogen peroxide, and lipid peroxidation. In a study conducted by Kaddouri et al. [46], heterocyclic compounds with pyrazole, thiazole, and pyridine moieties were prepared, and their antioxidant activity was evaluated using the DPPH assay. The compound with the best antioxidant activity exhibited an IC_{50} of 14.76 µM, a value very similar to that of vitamin C, with an IC_{50} of 11.36 µM. In addition, our previous studies of the antioxidant profile of PTHs structurally

related to **TTNF37** showed that this class of compounds is comparable and often better than standard antioxidants in DPPH, ABTS, TAOC, and •NO assays [29,30,47].

2.2.3. Antiproliferative Activity Against MRC-5 Cell Line

The cytotoxic activity of **TTNF37** against the MRC-5 cell line was evaluated by an MTT (3-(4,5-dimethylthiazol-2-yl)-2,5-diphenyl-2H-tetrazolium bromide) assay. The results of this assay are expressed as Growth Inhibition 50% (GI_{50}) values. In the case **TTNF37**, the GI_{50} value is evaluated to be more than 60 µM (>15.74 µg/mL). The effect of **TTNF37** on cell viability relative to the vehicle is shown in Figure S7.

2.2.4. Quorum-Sensing Inhibition Activity

The use of conventional antibiotics exerts an intense selective pressure on microbial populations by eliminating susceptible cells and allowing the survival and proliferation of resistant ones [48]. This pressure arises because antibiotics interfere with essential processes such as protein synthesis, DNA replication, and cell wall formation, causing bacteria to develop resistance mechanisms [49]. To overcome this problem, alternative strategies focused on QS are used to reduce virulence and pathogenicity without impairing bacterial growth, thereby minimizing the risk of recalcitrance [4].

To select appropriate **TTNF37** concentrations for QS inhibition assays, the inhibitory (MIC) activities were first determined. The MIC values obtained for **TTNF37** against *P. aeruginosa* PA14-WT and the biosensor *P. aeruginosa* PA14-R3 are presented in Table 5. The MICs were 800 µg/mL and 1000 µg/mL for strain *P. aeruginosa* PA14-WT and *P. aeruginosa* PA14-R3, respectively.

Table 5. MIC values of **TTNF37** against *P. aeruginosa* PA14-WT and biosensor PA14-R3.

	MIC (µg/mL)	
Compound	***P. aeruginosa* PA14-WT**	***P. aeruginosa* PA14-R3**
TTNF37	800	1000

The results of the QS inhibition screening performed using **TTNF37** in a range of different concentrations (6.25 to 1000 µg/mL), and of furvina and FC30 are depicted in Figure 2a and Figure S8, respectively. **TTNF37** interfered with the *P. aeruginosa* 3-oxo-C12-HSL-dependent QS system, and its effect was dose-dependent (around 26% to 98%). This is consistent with the premise that a compound that impairs QS without significantly affecting cell growth can be considered a promising inhibitor, as it typically shows a reduction in relative bioluminescence emission of at least 50% and a reduction in cell growth of no more than 20% [10]. Although our compound slightly exceeded this threshold with a 30% reduction in cell growth at all concentrations tested, it still showed potent QS inhibition. In particular, no growth inhibition occurs at 1000 µg/mL, which can be attributed to the high absorbance values displayed by the samples at this concentration. Indeed, **TTNF37** has an intense yellow/orange colour. When water was added to the compound prepared in DMSO (to attain a maximum of 6% *v*/*v* in the well), some precipitates were immediately formed. Nonetheless, this tends to be less evident or disappear over time. We also did a reading at 24 h of incubation instead of the usual 4 h period, and the results were more consistent. This confirms that the high absorbance values observed can be attributed to compound precipitation (see Figure S9 in the Supplementary Information). The compound color and precipitation affect only the absorbance readings (related to bacterial growth inhibition evaluation) and not bioluminescence. The effect of **TTNF37** on the production of 3-oxo-C12-HSL was also assessed (Figure 2b), and bioluminescence reductions between 21% and 56% were found. No reduction was observed at concentrations of 6.25 µg/mL

and 12.5 μg/mL. The levels of the 3-oxo-C12-HSL produced were also affected, with no autoinducer being detected from a 100 μg/mL concentration. However, particularly for the lower concentrations, the results of bioluminescence reduction and relative 3-oxo-C12-HSL were not uniform, as they did not follow a trend and were quite variable between concentrations. These results are consistent with those of Lidor et al. [50], who found that thiazolidinedione derivatives with different side carbon chains inhibited 3-oxo-C12-HSL production by up to 46%. For these analyses, the authors employed a modified β-Gal plate assay using the *E. coli* strain MG4 (pKDT17) and organic extracts from *P. aeruginosa*. Although Lidor's compounds have a different structure from our derivatives, this study emphasises the importance of the thiazole core in inhibiting HSL production in *P. aeruginosa*.

In relation to the effect of **TTNF37** on the autoinducer detection, the data show a dose-dependent activity with a maximum reduction of ca. 65% (Figure 2c). Nonetheless, it seems that lower concentration promoted better results. This could also be related to some precipitations of the compound at higher concentrations (as mentioned before). Interestingly, Ammar et al. [51] demonstrated that 2-oxo-pyridine derivatives inhibited LasR gene expression by 60%, highlighting the potential of pyridine-containing compounds to disrupt LasR-regulated QS. **TTNF37** demonstrated the ability to interfere with both production and detection mechanisms, with this effect slightly less pronounced on the 3-oxo-C12-HSL production.

2.2.5. Virulence Inhibition Activity

The establishment of *P. aeruginosa* infections strongly depends on the production of virulence factors that play a crucial role in bacterial colonisation and host tissue invasion. Among these factors, pyocyanin and pyoverdin are particularly important. Pyocyanin is a blue-green pigment produced by about 95% of *P. aeruginosa* strains [52]. This redox-active molecule modulates the host's immune response, increases bacterial resistance to environmental stress, and contributes to tissue damage and the spread of infection [11,53]. In addition to these effects, pyocyanin establishes a crucial link with pyoverdin in the context of iron metabolism and biofilm development. Within biofilms, pyocyanin-induced oxidative stress damages neighbouring bacterial and fungal cells, leading to the release of Fe^{3+} ions into the environment [52]. This increases the availability of iron, which is subsequently exploited by pyoverdin, a high-affinity iron chelator [54]. The iron uptake facilitated by pyoverdin promotes bacterial proliferation and increases pyocyanin production. However, pyocyanin in its reduced form converts Fe^{3+} into Fe^{2+}, which is less efficiently sequestered by pyoverdin [52]. Pyoverdin also increases bacterial resistance to toxic metals [55]. Although pyocyanin biosynthesis is primarily regulated by the pqs system, the las and rhl systems also play an important role. The las system positively regulates pqs, whereas the rhl system exerts an inhibitory effect, thereby modulating pyocyanin production. Furthermore, the las system also regulates the biosynthesis of pyoverdine, further emphasizing its role in iron homeostasis and virulence of *P. aeruginosa* [10].

TTNF37 demonstrated the ability to reduce to some extent the amount of pyocyanin produced, as can be observed in Figure 3. A maximum reduction of ~33% was acquired at 25 μg/mL. This result is consistent with the study by Li et al. [56], who developed various thiazole acid derivatives acting as IQS modulators analogs. The authors observed that the most effective compound (at 10 μM) led to a 30% reduction in pyocyanin production compared to wild-type *P. aeruginosa* PAO1. At higher **TTNF37** concentrations, no inhibition of pyocyanin production was observed. This may be partly due to a slight decrease in bacterial growth, which influences growth-normalised pyocyanin values. Furthermore, the compound's solubility may also interfere and contribute to the non-linear inhibition profile.

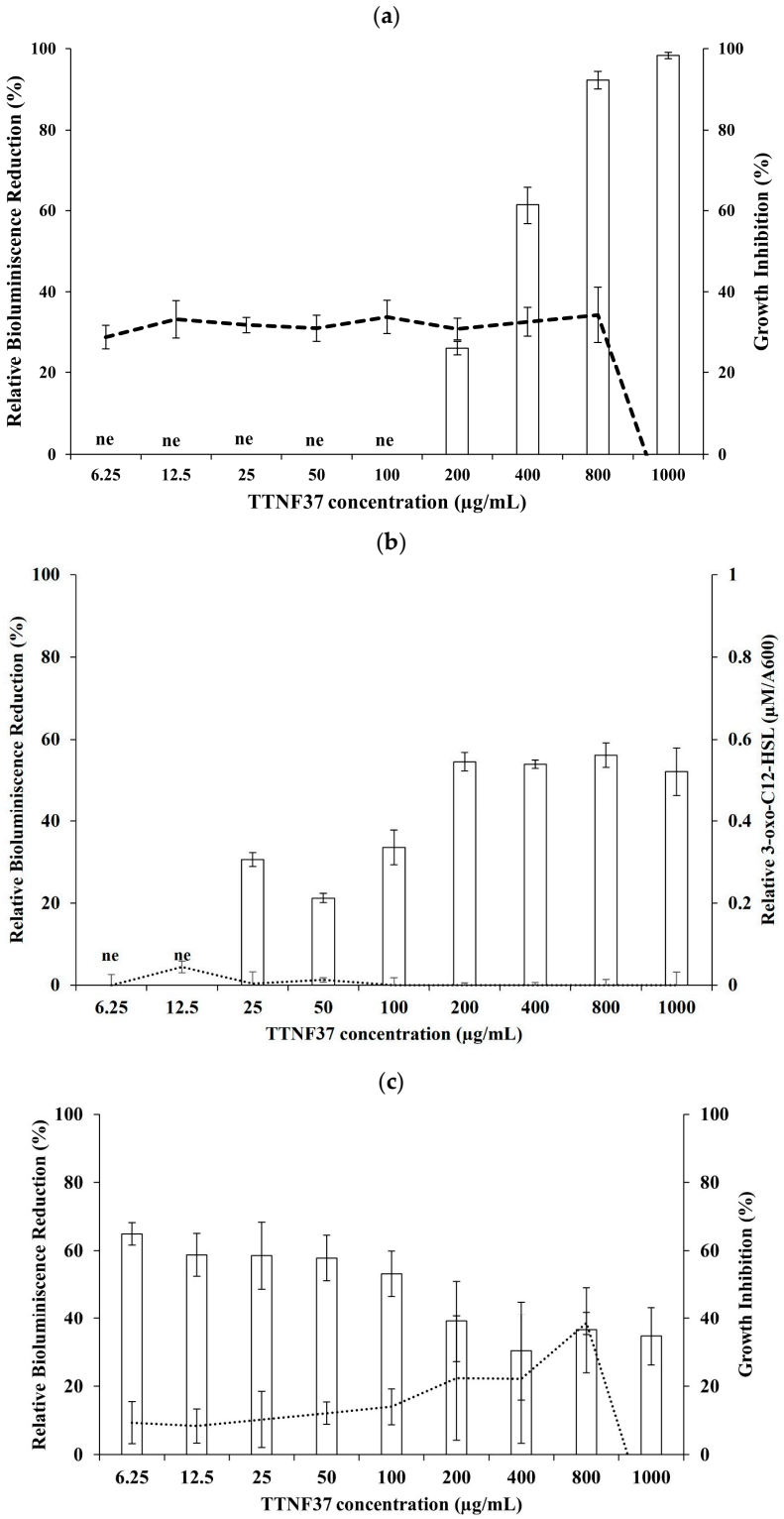


Figure 2. Effect of increasing concentrations of **TTNF37** (6.25 to 1000 µg/mL) on *P. aeruginosa* 3-oxo-C12-HSL-dependent QS system (shown by the bars) and growth inhibition (A_{600nm}, shown by the dotted line) (**a**). Effect of increasing concentrations of **TTNF37** (6.25 to 1000 µg/mL) on the production of 3-oxo-C12-HSL (shown by the bars) and quantification of the 3-oxo-C12-HSL produced levels (shown by the dotted line) (**b**). Effect of increasing concentrations of **TTNF37** (6.25 to 1000 µg/mL) on the detection of 3-oxo-C12-HSL (shown by the bars) and growth inhibition (A_{600nm}, shown by the dotted line) (**c**). Bioluminescence emissions were normalised to the cell density of the bacterial culture and expressed as a percentage of the untreated controls (relative bioluminescence). 3-oxo-C12-HSL levels were expressed as percentages relative to untreated controls (relative 3-oxo-C12-HSL); ne = no effect. Mean values ± standard deviations for at least three replicates are illustrated.

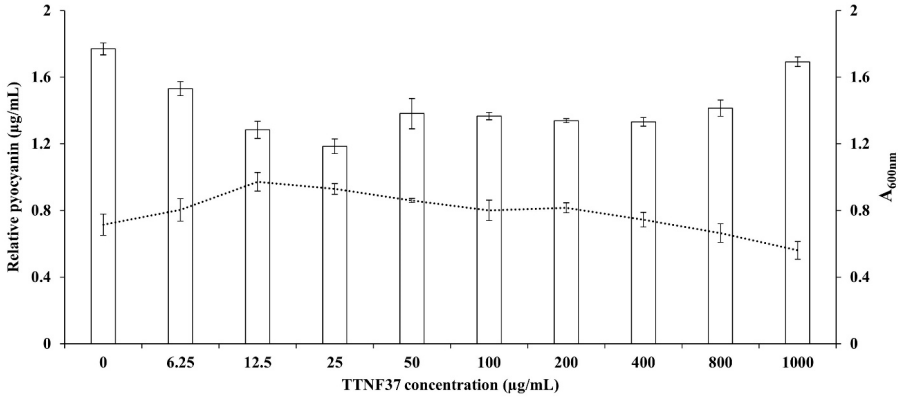


Figure 3. Influence of **TTNF37** on pyocyanin production (shown by the bars) and cell growth (A_{600nm}, shown by the dotted line) as a function of the different concentrations (6.25 to 1000 μg/mL). The levels of pyocyanin were measured in cell-free supernatants from cultures of the *P. aeruginosa* PA14-WT strain. Mean values ± standard deviations for at least three replicates are illustrated.

Apparently, **TTNF37** did not affect the pyoverdine production (Figure 4). Indeed, for the higher concentrations (800 and 1000 μg/mL), it was possible to observe a slight increase in the pyoverdine production, which could again be related to some precipitation of the compound at higher concentrations. Additionally, **TTNF37** can stimulate the production of pyoverdine by *P. aeruginosa*, or it can absorb at 400 nm, which was the wavelength used for pyoverdine quantification. This effect has already been observed with other molecules synthesized by our group [11], where the Co(III) complex based on PTH ligand (*E*)-2-(2-(pyridin-2-ylmethylene)hydrazinyl)-4-(*p*-tolyl)thiazole, showed no effect on pyoverdine production even at a concentration of 1000 μg/mL.

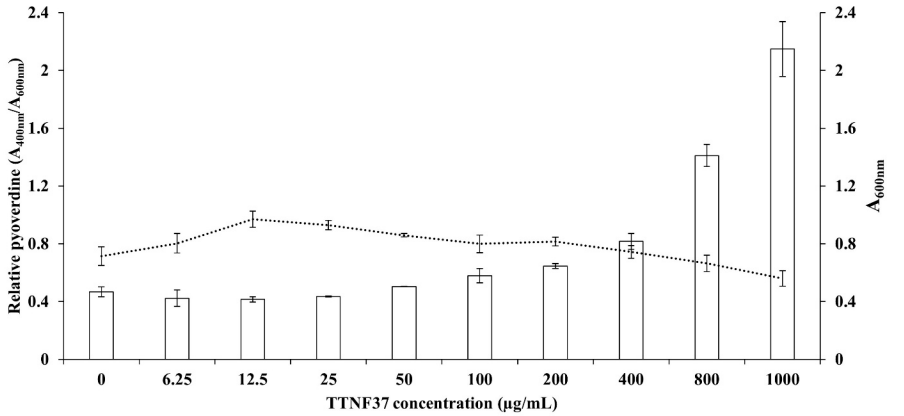


Figure 4. Influence of **TTNF37** on pyoverdine production (shown by the bars) and cell growth (A_{600nm}, shown by the dotted line) as a function of the different concentrations (6.25 to 1000 μg/mL). The levels of pyoverdine were measured in cell-free supernatants from cultures of the *P. aeruginosa* PA14-WT strain. Mean values ± standard deviations for at least three replicates are illustrated.

2.2.6. Biofilm Formation Inhibition Activity

P. aeruginosa forms structured biofilms that contribute to its persistence and high antibiotic recalcitrance in chronic infections. These microbial communities consist of cells that adhere to biotic or abiotic surfaces and are embedded in a self-produced extracellular polymeric matrix (EPS). Biofilm-associated bacteria can be up to 1000 times more resistant than their planktonic counterparts [57,58]. The regulation of biofilm formation in *P. aeruginosa* largely depends on QS, which plays a key role in the initial stages of cell–cell adhesion. For example, Lima et al. [59] demonstrated that 100% of the tested biofilm-producing *P. aeruginosa* strains were positive for the QS genes *rhlI*, *rhlR*, and lasR, with the *lasI* gene

detected in 97.5% of the strains, emphasising the important role of the las system in biofilm formation. Similarly, Hemmati et al. [60] found a significant correlation between QS genes and the ability to form biofilms in *P. aeruginosa* isolates. In particular, the authors found that biofilm-forming strains had high prevalence rates for the genes *rhlI* (84.3%), *rhlR* (94.7%), *lasI* (93.0%), and *lasR* (81.7%). In addition, it should be noted that 95.8% of the isolates tested in the study (120 clinical isolates in total) were capable of biofilm production, with 42.5% of them showing strong biofilm formation features.

The preventive action of **TTNF37** at different concentrations on biofilm formation by the *P. aeruginosa* PA14-WT strain was also studied. For this, its effect was evaluated in terms of reduction in biomass productivity (Figure 5), inhibition of the metabolic activity (Figure 6), and culturability (Figure 7) of the biofilm cells. A concentration-dependent effect was observed with biomass reduction from around 14% to 50%. A 38% reduction in maximum metabolic activity was achieved. Regarding biofilm cell culturability, a reduction of (1.55 Log (CFU/mL)) was attained from 100 µg/mL to 1000 µg/mL. A reduction of about 0.27 Log (CFU/mL) was obtained for the lowest concentration. It has been shown that compounds with anti-QS activity can inhibit biofilm formation. In particular, Mohammed et al. [61] synthesised a series of benzo[d]thiazole and 2-pyrazolo[1,5-a]pyrimidin-3-yl)benzo[d]thiazole derivatives and observed a significant inhibition of *P. aeruginosa* biofilm formation, with the highest reduction reaching 77%.

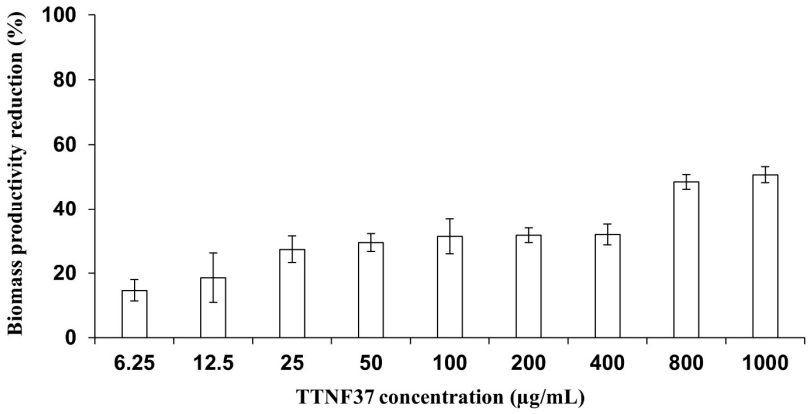


Figure 5. Preventive action of **TTNF37** at >MIC (1000 µg/mL), MIC (800 µg/mL), and sub-inhibitory concentrations (6.25 to 400 µg/mL) on biomass productivity of *P. aeruginosa* PA14-WT strain. Mean values ± standard deviations for at least three replicates are illustrated.

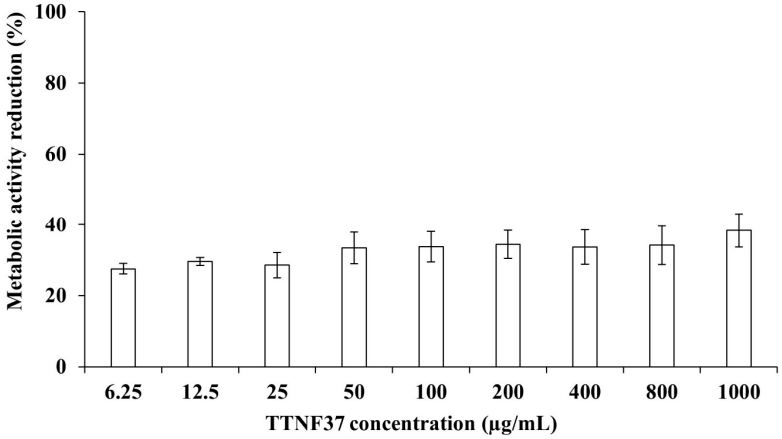


Figure 6. Effect of **TTNF37** at >MIC (1000 µg/mL), MIC (800 µg/mL), and sub-inhibitory concentrations (6.25 to 400 µg/mL) on metabolic activity of biofilm cells of *P. aeruginosa* PA14-WT strain. Mean values ± standard deviations for at least three replicates are illustrated.

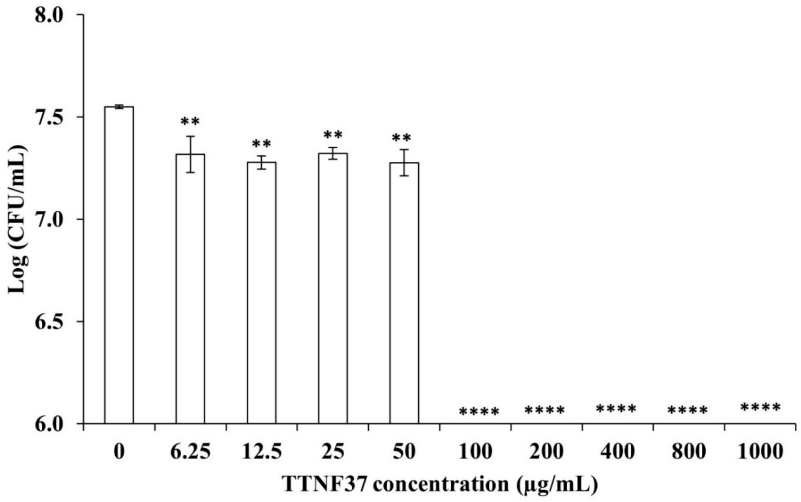


Figure 7. Effect of **TTNF37** at > MIC (1000 µg/mL), MIC (800 µg/mL), and sub-inhibitory concentrations (6.25 to 400 µg/mL) on culturability of biofilm cells of *P. aeruginosa* PA14-WT strain. For the 100–1000 µg/mL of **TTNF37**, no Log (CFU/mL) was detected. Culturable biofilm cells were below the detection limit of the plate counting method (i.e., 6 Log (CFU/mL)). Statistical significance is indicated as $p < 0.01$ (**), and $p < 0.0001$ (****) compared to biofilms without treatment. Mean values ± standard deviations for at least three replicates are illustrated.

2.2.7. Effect on Biofilm Structure and Membrane Integrity of Biofilm Cells

To further investigate the effect of **TTNF37** on PA14-WT biofilms, the structure and membrane integrity of biofilm cells were analysed using optical coherence tomography (OCT), fluorescence microscopy, and flow cytometry. These analyses were performed with **TTNF37** concentrations between 100 and 1000 µg/mL, as this range corresponded to the conditions where the most pronounced effects on biofilm culturability were observed. The OCT images revealed clear differences in biofilm structural organisation across the tested conditions. Control and DMSO-treated samples displayed irregular, heterogeneous biofilm structures, whereas biofilms formed in the presence of **TTNF37** exhibited a more uniform and less complex structure, particularly at higher concentrations (Figure 8). Moreover, the macroscopic images of the coupons, corresponding to the same field of view analysed by OCT, showed concentration-dependent differences in biofilm coverage. At the highest concentrations of **TTNF37** (800 and 1000 µg/mL), no macroscopically visible biofilm coverage was observed in the analysed area, and the coupon surfaces were practically free of adhering material. In contrast, at 100 µg/mL, the macroscopic appearance of the biofilm in the same field of view was comparable to that under control conditions (Figure 8). Notably, within the concentration range of 100–400 µg/mL, biomass showed only limited reduction despite the pronounced decrease in culturability. This is consistent with OCT and macroscopic observations, which indicate the persistence of surface-associated biofilm components, and reflects the fact that biomass measurements account for total biofilm material, rather than exclusively culturable cells.

To further characterise the observed biofilm structural alterations, OCT images were quantitatively analysed using the Biofilm Imaging and Structure Classification Automatic Processor (BISCAP). A pronounced reduction in average biofilm thickness was detected at **TTNF37** concentrations of 800 and 1000 µg/mL, with values decreasing from approximately 25 µm under control conditions to below 8 µm (Figure 9A). A similar trend was observed for maximum biofilm thickness, which decreased markedly at these concentrations, reaching values below 20 µm compared to approximately 150 µm in the untreated and DMSO controls (Figure 9B). Moreover, a notable effect was observed for biofilm roughness, with

values decreasing from approximately 25 in controls to 2 when biofilms were treated with **TTNF37** concentrations of 800 and 1000 μg/mL (Figure 9C).

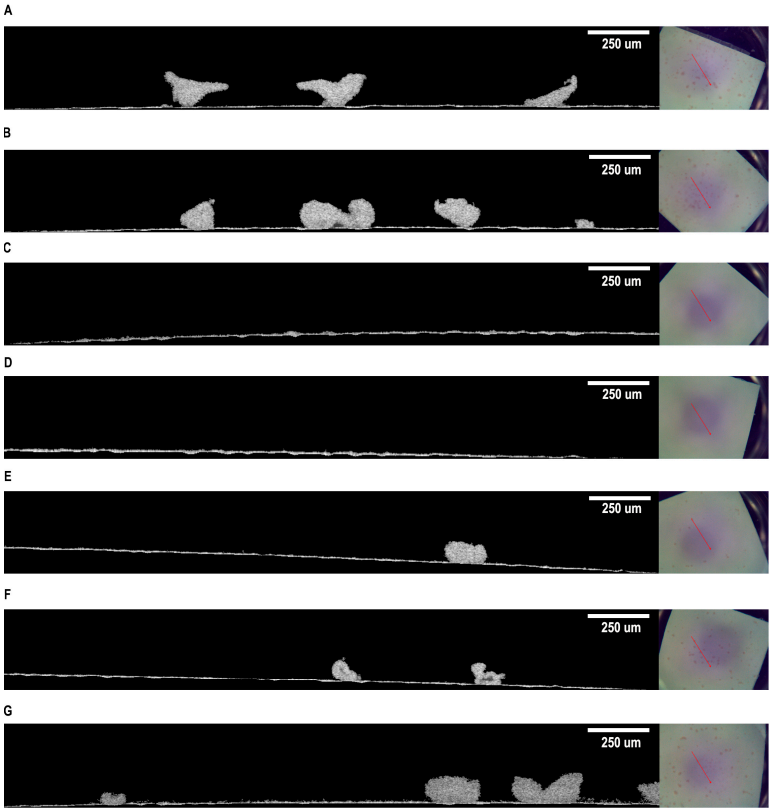


Figure 8. Representative images of the structure of 24 h-old *P. aeruginosa* PA14-WT biofilms formed in polystyrene coupons: in the absence of **TTNF37** and DMSO (**A**), in the presence of DMSO (**B**), and in the presence of **TTNF37** at different concentrations: 1000 (**C**), 800 (**D**), 400 (**E**), 200 (**F**), and 100 μg/mL (**G**). Images were acquired in the X-Z plane with a field of view of 3.66 × 2.98 mm^2, corresponding to a resolution of 1024 × 1024 pixels. Images on the right show representative photographs of the corresponding coupons after biofilm formation, where the red arrow indicates the region selected for biofilm imaging.

At intermediate concentrations, particularly 400 and 200 μg/mL, biofilm thickness and roughness parameters showed a partial reduction. In contrast, at 100 μg/mL, average and maximum thickness as well as roughness were comparable to the control, indicating a limited impact on biofilm structure.

Membrane integrity of PA14-WT biofilm cells was assessed by propidium iodide (PI) uptake using flow cytometry and by Live/Dead staining observed with epifluorescence microscopy (Figure S10). Across the tested **TTNF37** concentrations (100–1000 μg/mL), no significant increase in PI uptake was detected compared with the untreated and DMSO controls (Figure S10A), indicating that **TTNF37** does not affect the membrane integrity under these conditions. Fluorescence microscopy observations were consistent with the flow cytometry data, showing a predominance of green-stained cells across all conditions and no marked increase in red-stained cells following **TTNF37** treatment (Figure S10B). However, a visible reduction in the number of biofilm-associated cells was observed in the presence of **TTNF37**, including at 100 μg/mL, indicating a decrease in cellular density rather than loss of membrane integrity in the remaining adhered cells.

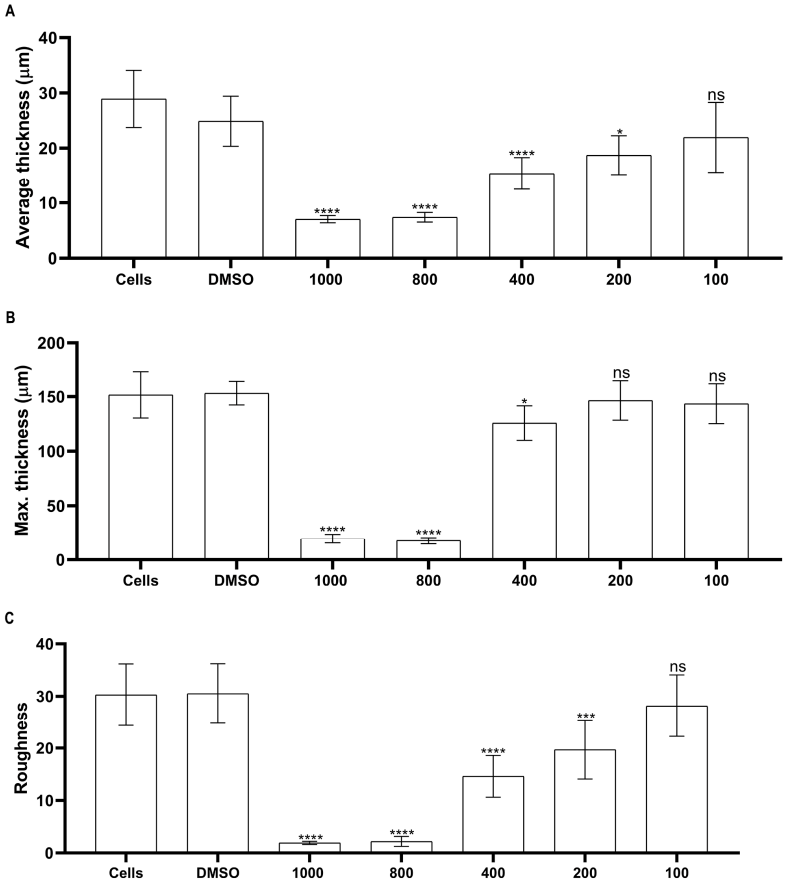


Figure 9. Effect of **TTNF37** (at 1000, 800, 400, 200, and 100 µg/mL) on biofilm average thickness (**A**), biofilm maximum thickness (**B**) and roughness (**C**) in *P. aeruginosa* PA14-WT. Biofilm thickness and roughness were measured in the presence and absence of **TTNF37**. Mean values ± standard deviations of three independent experiments are shown. Statistical significance is indicated as $p < 0.05$ (*), $p < 0.001$ (***), and $p < 0.0001$ (****), compared with the negative control (DMSO). ns not significant.

Considered together with the culturability, OCT, biomass, and metabolic activity data, these results indicate that **TTNF37** reduces the number of biofilm-associated cells and alters biofilm structure without exerting a membrane-disruptive effect in the adhered cells.

2.3. Evaluation of HSA Binding

HPAC (High-Performance Affinity Chromatography) analysis was performed to evaluate the binding of **TTNF37** to HSA, along with selected standard drugs that exhibit weak (paracetamol) and strong (flurbiprofen, loratadine, and naproxen) interactions with HSA [62–64]. The results are presented in Table 6.

Table 6. Obtained retention factors (k) for the tested compound and standards.

Compound	Retention Factor (k)
TTNF37	13.45 ± 0.21
Paracetamol	0.00 *
Flurbiprofen	11.75 ± 0.08
Loratadine	>35
Naproxen	>35

* Measured retention times were equal to the dead time within experimental resolution.

According to the obtained k values, flurbiprofen, loratadine, and naproxen exhibited stronger interactions with HSA than paracetamol, which is in accordance with the literature data [62–64]. For the tested compound, the k value was 13.45 (similar to flurbiprofen, but much lower than loratadine and naproxen), indicating a relatively strong interaction with HSA.

2.4. In Silico Analysis

LasI/R are molecular targets associated with QS; therefore, docking calculations are usually performed on these proteins [65,66]. Herein, we performed molecular docking analysis to assess if **TTNF37** targets LasI/R. Since **TTNF37** contains three groups that may undergo protolytic reactions (pyridine moiety, carboxyl group, and N–H), it is questionable in which exact form this molecule exists in physiological pH (pH = 7.40). Because of that, before docking, the prediction of pKa values for these three groups was made to determine the most dominant form of **TTNF37** present at physiological pH. Given the importance of HSA for the transport of antibacterial drugs through the bloodstream [31], interactions between **TTNF37** and this protein were also studied by molecular docking.

2.4.1. Prediction of pKa Values and Distribution of Micro Species

These calculations were performed using MarvinSketch [67]. The first pKa value (pKa_1 = 2.08) refers to the pyridine moiety, the second (pKa_2 = 5.77) corresponds to the carboxyl group, while the third (pKa_3 = 9.77) belongs to the N–H hydrogen atom. Analysis of the microspecies distribution diagram (Figure 10) indicates that **TTNF37** exists in its monoanionic form, which dominates the solution at pH 7.40 (97.26%), implying the presence of a deprotonated carboxyl group.

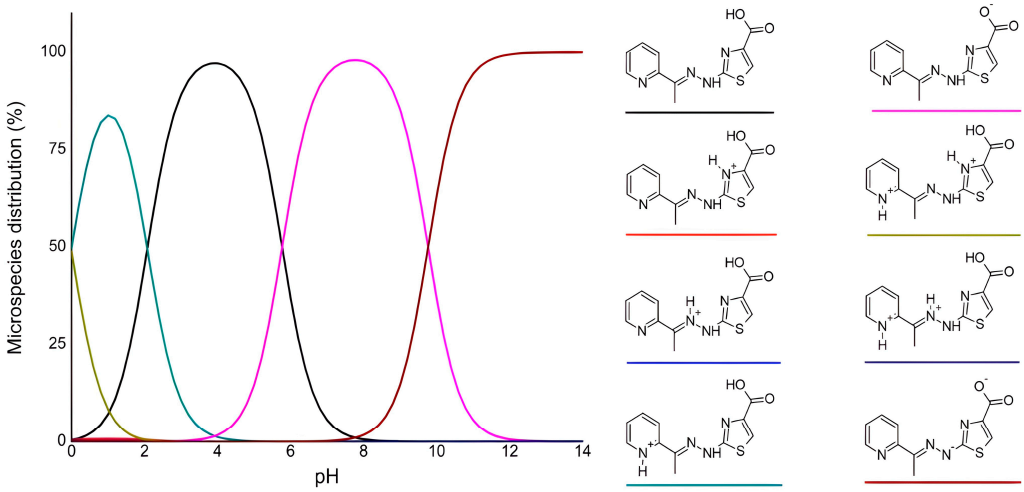


Figure 10. Microspecied distribution diagram of **TTNF37**.

2.4.2. Molecular Docking

This study aimed to evaluate the bioactive conformation through non-covalent interactions achieved by monoanionic **TTNF37** and estimate its binding affinity for target proteins. To assess the role of the methyl group in modulating activity, docking calculations were also carried out for the demethylated analogue of **TTNF37** (**1**) (Scheme 1). HSA is renowned for its versatile ligand-binding capabilities across numerous sites, accommodating a diverse array of molecules, ranging from endogenous and exogenous small compounds to larger peptides and proteins [68]. To compare intermolecular interactions and estimate binding energies with HSA, docking calculations were conducted, examining the binding of **TTNF37** alongside the known oral anticoagulant warfarin and the antipyretic ibuprofen. Furthermore, considering that HSA in real conditions does not have all active sites free,

a parallel study including FA-bound HSA was performed. Figure 11a–c illustrates the classical hydrogen interactions formed by the monoanion **TTNF37** in its estimated 3D bioactive conformation. At all three active sites of the HSA, **TTNF37** serves as an acceptor of classical hydrogen bonds, interacting with Lys199 (N–H···O and N–H···N, d = 2.358 and 1.864 Å, respectively), Ser192 (O–H···O, d = 2.175 Å), Asn391 (N–H···O, d = 2.090 Å) and Tyr161 (O–H···O, d = 2.100Å) (Figure 11).

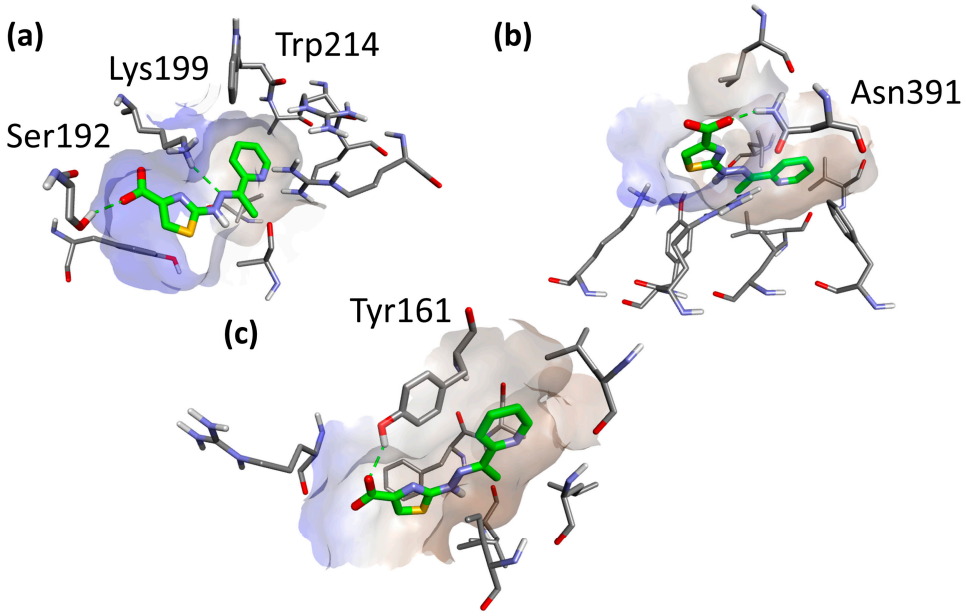


Figure 11. Three-dimensional bioactive conformations of monoanionic **TTNF37** bound in Sudlow site 1 (**a**), Sudlow site 2 (**b**), and drug-binding site 3 (**c**), with the ligand shown in thick licorice representation. Binding cavities are represented as surfaces, with hydrophobic regions in brown and hydrophilic regions in blue. Amino acids interacting with ligands via hydrogen bonds (dashed green lines) are depicted in capped sticks style and labelled with three-letter codes and sequence numbers. Atom colouring follows standardised CCDC conventions: ligand carbons (green), amino acid carbons (grey), oxygen (red), nitrogen (bluish-purple), sulfur (yellow) and hydrogen (white). The complete amino acid environment in the binding pocket is illustrated in the 2D plots generated using LIGPLUS [69]; however, it is omitted here for clarity.

The 2D plots generated using LIGPLOT v.2.2 8Ta [69] (Figure S11) show all the amino acids in the chemical space with which the mentioned molecules interact. A comprehensive analysis of intermolecular interactions reveals that **TTNF37** also engages with amino acids possessing nonpolar side chains, such as Ala, Trp, Leu, Gly, Phe, and Val, leading to the formation of aromatic and non-classical hydrogen interactions, confirming the amphiphilic nature of the ligand. Table 7 presents a comparison of the estimated binding affinities for the monoanion **TTNF37** and the mentioned co-crystallizers with which it crystallized the HSA protein. Docking calculations for co-crystallized molecules were examined using the same pose as in the crystal structures.

The clustering analysis of the 50 GA runs revealed a preferred binding mode for the ligand within the three distinct active sites of the HSA, as a function of estimated binding energy (Figure S12). The results indicate that the largest conformational population in Sudlow site 1 (Figure S12A) achieves an average binding free energy of -8.63 kcal mol^{-1}, whereas in Sudlow site 2 (Figure S12B), the estimated energy is higher at -9.42 kcal mol^{-1}. Notably, for drug binding site 3 (Figure S12C), the predominant conformational cluster exhibits a significantly more favourable binding energy of -13.40 kcal mol^{-1}, a finding consistent with the non-polar nature of this active site and the known high affinity of myristic acid for it. Additionally, **TTNF37**, characterised as a near-planar monoanionic

system, exhibits a considerably reduced degree of conformational freedom in comparison with co-crystalized ligands. However, Ligand Efficiency (LE) is a useful parameter in docking calculations as it assesses the binding energy contribution of each heavy atom in a ligand, helping to identify compounds with optimal binding affinity relative to their size [70]. Combining LE with clustering offers a better statistical and geometrical insight into the most favourable, bioactive conformation based on the RMSD cutoff and estimated binding energies. Based on the comparison of the binding affinity estimates obtained through cluster analysis of the aforementioned ligands and the calculated LE parameter, it can be concluded that the monoanion **TTNF37** exhibits slightly weaker but still comparable affinity to domains reserved for small organic molecules. However, it should be noted that GOLD's optimization is geared towards forecasting the probable binding pose of a ligand, rather than precisely calculating binding affinities. Further studies are needed to evaluate the stability and exact binding affinity of **TTNF37**@HSA fully.

Table 7. CHEMPLP total binding energies (E_{tot} in kcal mol^{-1}) and ligand efficiencies (LE in kcal mol^{-1} Heavy $Atom^{-1}$) for monoanionic **TTNF37**, **1**, and known co-crystallizers.

Ligand	PDB ID	Domain	Binding Site	E_{tot}	LE
TTNF37 anion	2BXD	IIA	Sudlow site 1	−8.63	−0.47
1 anion				−7.09	−0.41
Warfarin				−10.60	−0.48
TTNF37 anion	2BXG	IIIA	Sudlow site 2	−9.42	−0.52
1 anion				−7.95	−0.46
ibuprofen				−10.66	−0.71
TTNF37 anion	1BJ5	IB	Drug binding site 3	−13.40	−0.74
1 anion				−11.66	−0.68
Myristic acid				−14.01	−0.88

The same methodology was applied to the AHL Synthase LasI (PDB ID: 1RO5) and the LasR-3-oxo-C12-HSL transcription activator protein complex (PDB ID: 3IX3), systems involved in detecting and communicating cell density within bacteria through the signaling process known as quorum sensing. Table 8 summarizes the estimated binding affinities of the monoanionic **TTNF37**, 3-oxo-C12-HSL, and the known inhibitor furvina (G1).

Table 8. CHEMPLP total binding energies (Etot in kcal mol^{-1}) and ligand efficiencies (LE in kcal mol^{-1} Heavy $Atom^{-1}$) for monoanionic **TTNF37**, **1**, and co-crystallized 3-Oxo-C12-HSL, and known inhibitor furvina (G1).

Ligand	PDB ID	E_{tot}	LE
TTNF37 anion	3IX3	−11.22	−0.62
1 anion		−9.76	−0.57
3-Oxo-C12-HSL		−18.82	−0.90
furvina (G1)		−8.22	−0.68
TTNF37 anion	1RO5	−9.58	−0.53
1 anion		−7.50	−0.44
furvina (G1)		−6.93	−0.56

Docking calculations on LasR (PDB ID: 3IX3) estimated that the monoanion **TTNF37** binds with almost the same affinity as the known inhibitor furvina (G1), while the 3-Oxo-C12-HSL molecule binds with significantly higher affinity. This result is expected, given that furvina (G1) and the monoanion **TTNF37** are both small and nearly completely planar molecules. In contrast, the 3-Oxo-C12-HSL molecule has much greater conformational free-

dom and the potential to form a larger number of interactions, allowing it to crystallize with the protein. In the active site, the monoanion **TTNF37** forms four classical hydrogen bond interactions (Figure 12a): sa Tyr56 (O–H···O, *d* = 2.102 Å), Thr75 (O–H···O, *d* = 1.892 Å), Thr115 (O–H···O, *d* = 2.877 Å) and Ser129 (O–H···O, *d* = 2.088 Å). Based on the 2D plots (Figure S13) and a complete analysis of the chemical space, it has been determined that the monoanion **TTNF37** forms hydrophobic, non-classical interactions with the amino acid residues of Leu, Ile, Ala, Arg, Tyr, and Trp. Full cluster analysis results, including the conformational population of monoanionic **TTNF37**, based on 50 GA runs, are presented in Figure S14.

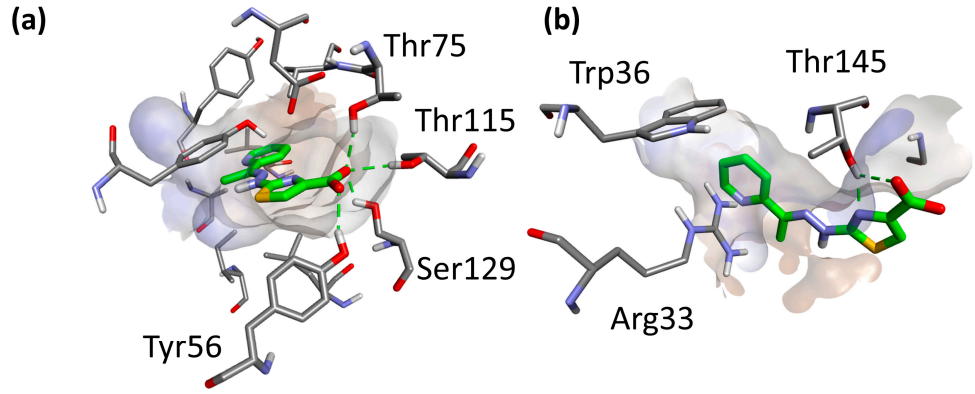


Figure 12. Three-dimensional bioactive conformations of monoanionic **TTNF37** canonical site of LasR (PDB ID: 3IX3; (**a**) and LasI-AHL synthase (PDB ID: 1RO5; (**b**), with the ligand shown in thick liquorice representation. Binding cavities are represented as surfaces, with hydrophobic regions in brown and hydrophilic regions in blue. Amino acids interacting with ligands via hydrogen bonds (dashed green lines) are depicted in capped sticks style and labelled with three-letter codes and sequence numbers. Atom colouring follows standardised CCDC conventions: ligand carbons (green), amino acid carbons (grey), oxygen (red), nitrogen (bluish-purple), sulfur (yellow) and hydrogen (white). The complete amino acid environment in the binding pocket is illustrated in the 2D plots generated using LIGPLUS [69], which are omitted here for clarity.

In the case of binding to LasI-AHL synthase (PDB ID: 1RO5), the monoanion **TTNF37** represents a dual acceptor for classical hydrogen interactions through the carboxylate oxygen and thiazole nitrogen atoms with Thr145 (O–H···O, *d* = 2.153 Å and O–H···N, *d* = 2.337 Å) (Figure 12b). The active site of this protein is enriched with hydrophobic amino acids, such as Phe, Val, and Gly, as observed in the 2D plot of intermolecular interactions (Figure S13). Therefore, the monoanion **TTNF37** orients its polar carboxylate anion toward the exterior of the protein, making the 2-acetylpyridine moiety more accessible for hydrophobic interactions.

Molecular docking studies with HSA revealed that **TTNF37** consistently exhibits more favorable docking energy scores than **1** across all investigated binding sites (Table 7). The most pronounced difference was observed at drug binding site 3, suggesting that the methyl group promotes improved accommodation of the ligand within the hydrophobic pocket through enhanced hydrophobic contacts and steric complementarity. Furthermore, a similar trend was observed for quorum-sensing-related targets, where **TTNF37** displayed more favorable binding energy scores toward both AHL synthase LasI and the transcriptional regulator LasR compared to **1** (Table 8).

Three-dimensional bioactive conformations, first GOLD cluster docked solutions (generated using LIGPLUS v.2.2. [69]), and cluster analysis of docking results of monoanionic **1** in the three mentioned distinct active sites of the HSA, as well as in LasR-OC12 HSL complex and AHL Synthase Lasl, are provided in Supplementary Information (Figures S15–S20). This consistent behavior across structurally distinct proteins indicates that methy-

lation contributes to improved molecular recognition and binding stability. Overall, the results highlight methylation as a key structural determinant that modulates and enhances the activity of **TTNF37** across multiple protein interaction targets.

The key finding, evaluated using docking calculations, reveals that the monoanion **TTNF37** can be transported by HSA at physiological pH with an affinity similar to that of the anticoagulant warfarin. For QS proteins, **TTNF37** is evaluated to bind with the same affinity as the known inhibitor furvina (G1). The structure of **TTNF37** gives it amphiphilic properties, with functional groups of different polarities at its periphery. This makes it well-suited for interacting with both hydrophobic and hydrophilic canonical sites. Given the focus of this study, these results represent relative but satisfactory binding affinities, and further research is needed to determine the precise binding energy and stability of the protein–ligand complexes.

2.4.3. Analyses of Molecular Dynamics Simulations

To validate and refine the docking-derived binding modes of monoanionic **TTNF37** in quorum-sensing proteins, we performed 1000 ns molecular dynamics (MD) simulations using Desmond for the LasR transcriptional regulator (PDB: 3IX3) and LasI-AHL synthase (PDB: 1RO5) complexes. These simulations were designed to assess conformational stability, interaction persistence, and the compatibility of **TTNF37**'s amphiphilic pharmacophore with the physicochemical environments of both binding sites.

Backbone RMSD trajectories (Figure S21) indicate that both protein–ligand complexes remained structurally stable over the microsecond timescale. The ligand RMSD, computed relative to the initial docking poses, exhibited an early transient rise (<3 Å), followed by equilibration within the first 200 ns, and then low deviation (between 0.5 and 1.5 Å) for the remainder of the trajectories. This behaviour supports that the docking poses are energetically favourable and dynamically robust in aqueous solution, with no sustained drift that would suggest pose collapse or egress from the pocket.

2D interaction maps generated from the MD trajectories (Figure S22) reveal that while the principal hydrogen bonds predicted by docking were largely preserved, subtle rearrangements and new contacts emerged during the simulation, reflecting the dynamic adaptability of **TTNF37** interacting proteins. LasR (3IX3): **TTNF37** retained three classical hydrogen bonds, notably with Tyr47 and Arg61, which were anticipated from docking. However, the interaction pattern shifted slightly, with non-classical and hydrophobic contacts involving Val76 becoming more prominent. Additionally, water-mediated bridges with Arg71 reinforced the hydrogen-bond network without displacing the ligand from its preferred orientation, suggesting a stable yet flexible binding mode.

LasI (1RO5): **TTNF37** maintained a water-mediated hydrogen bond via its carboxylate oxygen to Thr145, confirming the importance of this residue as predicted by docking. Interestingly, new hydrogen bonds formed with Arg33 and Phe105, indicating adaptive engagement with the binding pocket. The hydrophobic character of the LasI site (enriched in Phe, Val, Trp) promoted sustained packing of the 2-acetylpyridine moiety, while the carboxylate anion remained partially solvent-exposed, in line with its docking orientation.

TTNF37 largely retained its near-planar conformation in the LasI binding site, with minor rotameric adjustments in the LasR binding site, leading to optimized hydrogen bonding and hydrophobic complementarity. These observations further underscore **TTNF37**'s amphiphilic design, enabling simultaneous engagement of polar and non-polar microenvironments. The persistence of key interactions, combined with the emergence of additional stabilizing contacts, suggests that **TTNF37** can adapt dynamically to the binding pocket while maintaining its bioactive pose.

Docking predicted that **TTNF37** binds LasR with an affinity comparable to furvina (G1) and engages LasI through dual hydrogen-bond acceptor interactions. MD simulations corroborate these hypotheses under explicit solvent conditions, while revealing interaction plasticity that enhances stability. Together, these findings strengthen the mechanistic picture of **TTNF37** as a viable quorum-sensing modulator, capable of durable engagement and adaptive binding in more biologically relevant environments.

3. Materials and Methods

3.1. Chemistry

3.1.1. Reagents and Apparatus

2-acetylpyridine (98%) and thiosemicarbazide (99%) were purchased from Acros Organics (Geel, Belgium), and bromopyruvic acid was purchased from Sigma-Aldrich (St. Louis, MO, USA). All employed solvents were of reagent grade and purchased from commercial suppliers. The solvents are used without further purification. Elemental analysis (C, H, N, S) was performed using the standard micro-methods on an ELEMENTAR Vario EL III CHNS/O analyzer (Elementar Analysensysteme GmbH, Langenselbold, Germany). IR spectrum of **TTNF37** was recorded in the MID region (4000−400 cm^{-1}) on a Thermo Scientific Nicolet 6700 FT-IR spectrometer (Thermo Fisher Scientific, Waltham, MA, USA) by the Attenuated Total Reflection (ATR) technique. Abbreviations used for IR spectroscopy: vs. (very strong), s (strong), m (medium), w (weak), and vw (very weak). ^{1}H and ^{13}C NMR spectra of **TTNF37** were recorded in DMSO-d_6 using a Bruker Avance 500 (Bruker, Bremen, Germany), while 2D NMR spectra (COSY, HSQC, and HMBC) were recorded in DMSO-d_6 using Varian/Agilent 400 (Agilent Technologies, Santa Clara, CA, USA). Tetramethylsilane (TMS) was used as an internal standard for ^{1}H and ^{13}C, and chemical shifts were given relative to it on the δ scale. Abbreviations used for NMR spectroscopy: s (singlet), d (doublet), dd (doublet of doublets), td (triplet of doublets). The structure is input in SMILES format. The pKa values of **TTNF37** and the distribution of microspecies were predicted using MarvinSketch (Version 21.17.0). [67].

3.1.2. Synthesis of 2-{(2E)-2-[1-(Pyridin-2-yl)ethylidene]hydrazinyl}-1,3-thiazole-4-carboxylic Acid

Solid bromopyruvic acid (0.07 g, 0.42 mmol) was added to the suspension of 2-acetylpiridine thiosemicarbazone (0.081 g, 0.42 mmol) in the mixture of water and ethanol (20 mL, 3:1, v/v). The reaction mixture was stirred for 24 h at room temperature. The ocher product was filtered off and washed with cold water, ethanol, and diethyl ether. The pure product was obtained by vapor diffusion of ethanol into the DMSO solution of the crude product. Yield: 0.089 g (82%). Anal. Calcd for $C_{11}H_{10}N_4O_2S$ (%): C, 50.37; H, 3.84; N, 21.36; S, 12.23. Found: C, 50.58; H, 3.96; N, 21.12; S, 12.42. FTIR (ATR, ν_{max}/cm^{-1}): 3171 (m), 3122 (s), 3006 (m), 2965 (m), 2854 (m), 2721 (w), 2623 (w), 2519 (w), 2439 (w), 1718 (s), 1680 (m), 1604 (m), 1577 (vs), 1516 (m), 1465 (s) 1438 (s), 1367 (w), 1339 (w), 1290 (m), 1223 (s), 1151 (m), 1106 (m), 1083 (w), 1045 (w), 991 (w), 954 (w), 919 (w), 853 (vw), 779 (m), 729 (m), 662 (w), 556 (w), 493 (w).

3.2. Biological Activity

3.2.1. Solutions Preparation

The **TTNF37** stock solution was prepared in DMSO (Fisher Scientific, Gillingham, UK) under sterile conditions, and serial dilutions were prepared when needed. The percentage of DMSO never exceeded 6% (v/v) of the final volume of the cell suspension. Erythromycin (a bacterial inhibitor), amphotericin (a fungal and yeast inhibitor), as well as (*Z*-)-4-bromo-5-(bromomethylene)-2 (5*H*)-furanone (FC30, QSI) and furvina (QSI, previously investigated

by our research group), were used as positive controls in the assays. All positive controls were prepared in DMSO.

3.2.2. Screening of the **TTNF37** Antimicrobial Activity

To evaluate the antimicrobial profile of **TTNF37**, the MIC against a range of microorganisms (listed in Table 9) was determined using the broth microdilution method described by Clinical Laboratory Standard Institute (CLSI) [71]. Antimicrobial activity was determined using Mueller–Hinton broth for bacteria and Sabouraud dextrose broth for yeasts and fungi. Solutions of the control compounds (stock concentration, 250 µg/mL) and the test molecule **TTNF37** (stock concentration, 1000 µg/mL) were prepared in DMSO. The direct colony method was used in preparation of suspension of bacteria and yeasts in sterile 0.9% saline, while the process of preparing the suspension of fungal spores included gentle stripping of spore from agar slants with growing aspergilli into sterile 0.9% saline. Suspension turbidity evaluation was conducted by comparison with 0.5 McFarland's standard. The 96-well plates were prepared by dispensing 100 µL of Mueller–Hinton broth for bacteria and Sabouraud dextrose broth for yeasts and fungi into each well, then 100 µL of the tested compound was added to the first well of each row, and the content was diluted twice by using a multichannel pipette. A 10 µL of diluted bacterial, yeast, or spores suspension was added to each well to give a final concentration of 5×10^5 CFU/mL for bacteria and 5×10^3 CFU/mL for fungi and yeast. Erythromycin served as a positive control for bacteria, while amphotericin B served as a positive control for yeasts and fungi. The inoculated plates were incubated at 37 °C for 24 h for bacteria and at 28 °C for 48 h for the yeasts and fungi. The bacterial growth was visualized by adding 10 µL of 10% solution of resazurin. The minimum inhibitory concentration (MIC) was defined as the lowest concentration that inhibited bacterial growth (the blue color of resazurin appeared).

Table 9. Microorganisms used in this study.

Assay	Microorganism Type	Strain	ATCC Reference
Antimicrobial profile	Gram-negative bacteria	*Escherichia coli*	25922
		Pseudomonas aeruginosa	9027
		Proteus hauseri	13315
		Klebsiella pneumoniae	10031
		Salmonella enterica subsp. *enterica serovar Enteritidis*	13076
	Gram-positive bacteria	*Staphylococcus aureus*	6538
		Clostridium sporogenes	19404
		Micrococcus luteus	4698
		Micrococcus luteus	10240
		Bacillus subtilis	6633
	Yeast	*Candida albicans*	10231
		Saccharomyces cerevisiae	9763
	Fungus	*Aspergillus brasilliensis*	16404
QS activity	Gram-negative bacteria	*P. aeruginosa* PA14	Wild-Type
		P. aeruginosa PA14-R3	LasI mutant carrying the PrsaL: luxCDABE transcriptional fusion integrated into the chromosome at the neutral attB site

3.2.3. Screening of the **TTNF37** Antioxidant Activity

The antioxidant capacity of **TTNF37** and Vitamin C, as a standard antioxidant, was evaluated in four spectrophotometric (ABTS, DPPH, NO, and TAOC) and two fluorometric (HORAC and ORAC) assays. The principles of these assays are outlined in the review book edited by Stengel and Connan [72], while detailed experimental procedures are presented in our recent publications [47,73]. The main information about assays is given in Table 10.

Table 10. Antioxidant assays used in this study.

Assay Abbreviation	Full Name of the Antioxidant Assay	Radical	Radical Generation Method	Result of the Assay
DPPH	2,2-diphenyl-1-picrylhydrazyl radical scavenging	DPPH$^{\bullet}$	Radical itself	IC_{50}
ABTS	2,2′-azino-bis(3-ethylbenzothiazoline-6-sulfonic acid radical scavenging	$ABTS^{+\bullet}$	The reaction of ABTS with $K_2S_2O_8$ in water	IC_{50}
NO	Nitric oxide scavenging	$^{\bullet}NO$	Incubation of $Na_2[Fe(CN)_6]$ solution in light	IC_{50}
HORAC	Hydroxyl Radical Antioxidant Capacity	$^{\bullet}OH$	Reaction between H_2O_2, CoF_2, and picolinic acid	TE
ORAC	Oxygen Radical Absorbance Capacity	$^{\bullet}OOH$	Thermal homolysis of 2,2′-azobis (2-amidinopropane) dihydrochloride	TE
TAOC	Total Antioxidant Capacity Assay	/	Reduction of Mo(VI) to Mo(V), with the subsequent formation of a stable blue-green phosphate Mo(V) complex at acidic pH	EC_{50}

IC_{50} value is the sample concentration required for a 50% free radical scavenging inhibition activity. EC_{50} value is the concentration of the investigated compound that results in an absorbance of 0.500. TE (Trolox equivalent) values are obtained from the equation: AUC_S/AUC_T, where AUCs = AUC(sample) − AUC(buffer blank) and AUC_T = AUC(Trolox) − AUC(buffer blank) (AUC means the net area under the curve).

3.2.4. MRC-5 Cell Culture

Lung fibroblast, a non-tumorigenic human cell line, MRC-5 (ATCC® CCL-171™), is cultured in a Minimum Essential Medium, according to ATCC recommendations. The medium was supplemented with 10% (*v*/*v*) fetal bovine serum (FBS), 2 mM L-glutamine, and antibiotics (100 U/mL penicillin and 100 µg/mL streptomycin). Cells were maintained in a humidified incubator at 37 °C with 5% CO_2 and routinely subcultured at 70–80% confluency using standard trypsin-EDTA procedures. To ensure the quality of culture, the MRC-5 cell line was regularly tested for mycoplasma contamination using PCR-based detection methods.

3.2.5. Screening of the **TTNF37** Anti-QS Activity

The ability of **TTNF37** to interfere with the QS response of *P. aeruginosa* was investigated by co-cultivation of the biosensor strain *P. aeruginosa* PA14-R3 and the wild-type

strain *P. aeruginosa* PA14 [74]. PA14-R3 recognises 3-oxo-C12-HSL and activates the expression of the lux*CDABE* operon in response. This leads to the production of luciferase (luxAB), which in turn causes light emission through an oxidation process. Since PA14-R3 does not synthesise natural autoinducers, bioluminescence only occurs when 3-oxo-C12-HSL is produced by the wild-type PA14 strain or artificially added. After the growth of *P. aeruginosa* PA14-WT and *P. aeruginosa* PA14-R3 on LBA plates, some colonies were scraped from the plate surfaces and diluted in LBB. Then A_{600nm} was adjusted to 0.045 (5.80×10^7 CFU/mL) and 0.015 (2.15×10^7 CFU/mL) for *P. aeruginosa* PA14-R3 and *P. aeruginosa* PA14-WT, respectively (reporter/wild-type ratio of 3:1). Subsequently, 180 µL of the co-culture and 20 µL of **TTNF37** (6.25 to 1000 µg/mL) were distributed in black and transparent flat opaque-bottomed, 96-well polystyrene (PS) microtiter plates. Furvina (12.5 µg/mL) and FC30 (2.5 µg/mL) were used as positive controls. Finally, light counts per second (LCPS) and A_{600nm} were measured after 4 and 24 h of growth using a microplate reader. The luminescence values were normalised by dividing the LCPS values by the A_{600nm} values.

3.2.6. Anti-QS Mode of Action of **TTNF37**

The effect of **TTNF37** on the production of AI 3-oxo-C12-HSL was evaluated according to Leitão et al. [10]. After the growth of *P. aeruginosa* PA14 (24 h at 37 °C in LBA), some colonies were collected by scraping the plate surfaces and diluted in LBB. Then the A_{600nm} of the cell suspension was adjusted to 0.05 (5.85×10^7 CFU/mL), and 9 mL of the suspension was added to 50 mL centrifuge tubes together with 1 mL of **TTNF37** (6.25–1000 µg/mL). After incubation (37 °C, 16 h, and 150 rpm), the A_{600nm} was measured to monitor cell growth. The remaining cell suspension was centrifuged at 3772 g for 20 min, and the supernatant was collected and filtered through a 0.22 µm pore size filter (Whatman, Maidstone, England). A suspension of PA14-R3 cells was then prepared, with some colonies diluted in LBB to an A_{600nm} of 0.045. The 96-well PS microtiter plates, with either a black opaque bottom or a transparent bottom, were filled with 180 µL of the previously prepared R3 suspension and 20 µL of supernatant. Cell suspensions with DMSO and without **TTNF37** were used as negative controls, and cell suspensions with FC30 (2.5 µg/mL) and furvina (12.5 µg/mL) were used as positive controls. After 4h of incubation, the LCPS and A_{600nm} were measured using a microplate reader. The luminescence values were normalised by dividing the LCPS values by the A_{600nm} values. For the calculation of 3-oxo-C12-HSL in each culture supernatant, a calibration curve was established by growing *P. aeruginosa* PA14-R3 in the presence of increasing concentrations of synthetic 3-oxo-C12-HSL.

A similar protocol was used to evaluate the effect of **TTNF37** on the detection of AI 3-oxo-C12-HSL [15]. After the growth of *P. aeruginosa* PA14-R3 (24 h at 37 °C on LBA plates), some colonies were collected by scraping and diluted in LBB. Then the A_{600nm} was adjusted to 0.05 (5.85×10^7 CFU/mL), and 9 mL of the cell suspension was added to 50 mL centrifuge tubes together with 1 mL **TTNF37** (6.25–1000 µg/mL). After incubation (37 °C, 16 h, and 150 rpm), the A_{600nm} was measured to monitor cell growth. The remaining cell suspension was adjusted to an A600nm value of 0.045. Subsequently, 96-well PS microtiter plates with black opaque bottom and with transparent bottom were filled with 180 µL of PA14-R3 cell suspension together with 20 µL of synthetic HSLs (at 25 µM). Cell suspensions with DMSO and without **TTNF37** were used as negative controls, and FC30 (2.5 µg/mL) and furvina (12.5 µg/mL) as positive controls. After 4h of incubation, LCPS and A_{600nm} were measured using a microplate reader. The luminescence values were normalised by dividing the LCPS values by the A_{600nm} values.

3.2.7. Screening of the TTNF37 ACTIVITY on the Production of QS-Related Virulence Factors

Pyocyanin and pyoverdine were extracted from the supernatants of cultures resulting from the assay in which the production of AI 3-oxo-C12-HSL was evaluated [75]. In brief, the A_{600nm} suspension of wild-type PA14 was adjusted to 0.05 (5.85×10^7 CFU/mL) and cultured in the presence of **TTNF37** at various concentrations (6.25 to 1000 µg/mL). After incubation (at 37 °C and 150 rpm for 16 h), the cells were collected by centrifugation (15 min at 12,000× g), and the culture supernatant was obtained.

Pyocyanin Assay

A mixture of 3 mL of chloroform with 5 mL of culture supernatant was used to extract pyocyanin. The chloroform layer (commonly reddish in colour) was transferred to a new glass tube. Then, a second extraction was performed with 1 mL of 0.2 M hydrochloric acid (HCl; Fisher Chemical, Geel, Belgium), and the upper layer was transferred to a 96-well plate with a clear bottom. Finally, A_{520nm} was measured using a microplate reader. The amount of pyocyanin (µg/mL) was calculated by multiplying the A_{520nm} values by 17.072 and normalised by dividing the A_{520nm} values by the A_{600nm} values [$(A_{520nm}/A_{600nm}) \times 17.072$].

Pyoverdine Assay

Pyoverdine production was assessed using a spectrophotometric approach adapted from the method described by Höfte et al. [76], with slight modifications. In brief, the pyoverdine concentration in the culture supernatant was determined by measuring the A_{400nm}. To estimate relative pyoverdine production, the A_{400nm} values were divided by the A_{600nm} values of the cultures [77].

3.2.8. Biofilm Prevention Assays

The ability of **TTNF37** to prevent biofilm formation of *P. aeruginosa* PA14-WT was evaluated as described by Leitão et al. [50]. In brief, after overnight incubation in LBB, the A_{620nm} of the cell suspension was adjusted to 0.04 ± 0.02 (4.9×10^7 CFU/mL). Subsequently, 96-well transparent-bottom microtiter plates were filled with 180 µL of the prepared suspension and 20 µL of **TTNF37** at concentrations ranging from 6.25 to 1000 µg/mL. After incubation at 37 °C and 150 rpm for 24 h, the contents of each well were discarded, and the wells were washed with saline (0.85% NaCl) to remove non-adherent or weakly adherent cells. The biofilm cells were then analysed for biomass using crystal violet staining (CV; Merck, Darmstadt, Germany), for metabolic activity using alamar blue staining (Sigma-Aldrich), and for culturability using colony-forming unit (CFU).

For biofilm structural characterisation and membrane integrity analysis, biofilms were also formed on sterile white polystyrene coupons (1 × 1 cm) placed in 24-well plates. Coupons were cleaned and sterilised before use according to established procedures [78]. Each well was filled with 900 µL of the adjusted bacterial suspension and 100 µL of **TTNF37** at the specified concentrations. Plates were incubated at 37 °C and 150 rpm for 24 h under the same conditions as previously described. After incubation, the coupons were gently washed with sterile saline to remove planktonic cells. The thickness and roughness of PA14-WT biofilms were then analysed by OCT, and membrane integrity was assessed by fluorescence microscopy and flow cytometry.

Biomass Production

The adherent bacteria were fixed with 250 µL of 99% ethanol (Diprolar, Odivelas, Portugal) for 15 min. The wells were then emptied, and the plate was air-dried at room temperature for 5 min. To stain the biofilm cells, 200 µL of 1% (*v*/*v*) CV solution was added

to each well of a 96-well plate and incubated for 5 min. After staining, the excess dye was carefully removed. The remaining CV was then dissolved with 200 µL of 33% (*v*/*v*) glacial acetic acid solution (ChemLab, Zedelgem, Belgium). The A_{570nm} was measured using a microtiter reader, and the quantification of biomass was determined according to Leitão et al. [54] using the following Equation (1):

$$\text{Biomass production reduction}(\%) = \frac{Ac - Aw}{Ac} \quad (1)$$

where Ac is the A_{570nm} of untreated biofilms, and Aw is the A_{570nm} for biofilms formed by bacterial cells exposed to the **TTNF37**.

Metabolic Activity

The wells with the adherent bacterial biofilms were filled with 190 µL of fresh MHB medium and 10 µL of an alamar blue (also known as resazurin) indicator solution (0.4 mM) prepared in sterile distilled water. In the presence of metabolically active cells, resazurin, a non-fluorescent blue dye, is reduced to resorufin, which is fluorescent and appears pink. After 4 h of incubation in the dark at 37 °C, fluorescence was measured using a microplate reader (λexcitation = 570 nm, λemission = 590 nm). The percentage of metabolic activity reduction (%MAR) was calculated according to Borges et al. [79] using the following Equation (2):

$$\text{Metaboli activity reduction}(\%) = \frac{FLc - FLw}{FLc} \quad (2)$$

where FLc is the fluorescence intensity value of untreated biofilms, and FLw is the fluorescence intensity value for biofilms formed by bacterial cells exposed to the **TTNF37**.

Biofilm Culturable Cells

After 15 min of incubation with the neutraliser, the biofilm cells were collected by scraping the bottom of the wells and resuspended in 200 µL of sterile saline (this procedure was repeated three times). The contents of each well were transferred to sterile microcentrifuge tubes, and serial 10-fold dilutions were prepared in saline. Finally, 10 µL of each dilution was plated on plate count agar (PCA, VWR, Leuven, Belgium) and incubated at 37 °C for 24 h. Then, CFU was counted (if 10 < CFU < 200) and the results were expressed as CFU *per* square centimetre of well area (CFU cm^{-2}) according to Vieira et al. [80] and following Equations (3) and (4):

$$\frac{CFU}{mL} = \frac{N}{SV \times Dilution} \quad (3)$$

where N is the number of CFU on the PCA plates, and SV is the sample volume in mL.

$$\frac{CFU}{Cm^2} = \frac{\frac{CFU}{mL} \times WV}{Wa} \quad (4)$$

where WV is the working volume of the well (0.2 mL), and Wa is the area of the well in cm^2 (1.53).

Thickness and Roughness

Biofilm structural characterisation was analysed by OCT according to Leitão et al. [78]. After incubation and washing, each coupon was immersed in 1 mL of sterile NaCl solution (0.85%) before image acquisition. The images were acquired with a Thorlabs Ganymede spectral domain OCT system (Thorlabs GmbH, Dachau, Germany) with a central wavelength of 930 nm and a field of view of 3.66 × 2.98 mm^3 in the X-Z plane

(1024 × 1024 pixels). For each coupon, at least five distinct regions were imaged to ensure representative sampling and reproducibility. Automated processing and quantitative analysis of the 2D OCT images were performed using the Biofilm Imaging and Structure Classification Automatic Processor (BISCAP, version 1) [81]. For each experimental condition, a minimum of five OCT images were analysed per independent experiment.

Membrane Integrity of Biofilm Cells

The membrane integrity of PA14-WT biofilm cells was evaluated using the Live/Dead BacLight™ Viability Kit (SYTO9™ and PI) (Invitrogen/Molecular Probes, Thermo Fisher Scientific; Eugene, OR, USA) [54]. This staining method differentiates cells with intact and compromised membranes based on dye permeability. SYTO9™ penetrates bacterial cells independently of membrane integrity, emitting green fluorescence, whereas PI selectively enters cells with damaged membranes and emits red fluorescence upon binding to double-stranded nucleic acids.

Briefly, the biofilm cells were recovered from coupons after 24 h of exposure to **TTNF37** at 37 °C and separated using a vortex in sterile NaCl solution. For each condition, the resulting cell suspensions were collected in final volumes of 950 µL and 700 µL for flow cytometry and epifluorescence microscopy analyses, respectively. For flow cytometry, the biofilm cell suspension was stained with 50 µL of PI (0.074 mM) and incubated for 7 min at room temperature in the dark. Samples were analysed using a CytoFLEX flow cytometer (model V0-B3-R1, Beckman Coulter, Brea, CA, USA) equipped with a PC5.5 filter. Data acquisition and analysis were performed using CytExpert software (version 2.4.0.28). Membrane integrity was evaluated based on PI fluorescence intensity. For epifluorescence microscopy, the biofilm cell suspension was stained with 250 µL of SYTO9™ (0.0123 mM) and 50 µL of PI (0.074 mM), followed by incubation for 7 min at room temperature in the absence of light. After staining, samples were filtered through polycarbonate membranes with a pore size of 0.22 µm. The membranes were mounted on microscope slides and examined using a LEICA DMLB2 epifluorescence microscope (LEICA Microsystems Ltd., Wetzlar, Germany). Observations were performed using a multi-band fluorescence filter set (excitation 480–500 nm, emission 485 nm). Images were acquired with a digital colour camera coupled to IM50 software (version 4.2.0) using a 100× oil immersion fluorescence objective.

3.3. HSA Binding—Preparation of Solutions and Chromatographic Conditions

TTNF37 and the standards (paracetamol, flurbiprofen, loratadine, and naproxen) were dissolved in DMSO (1 mg/mL) and diluted with the mobile phase to a final concentration of 0.2 mg/mL, then analyzed in duplicate. HPAC (High-Performance Affinity Chromatography) analysis was performed on an Agilent 1200 Series chromatograph (Agilent Technologies, Santa Clara, CA, USA), as previously described [82]. The retention behavior of tested compounds was investigated on an immobilized CHIRALPAK® HSA HPLC column (4 × 100 mm, 5 µm particle size) purchased from Daicel Chiral Technologies (Illkirch-Graffenstaden, France). The mobile phase was a mixture of ammonium acetate buffer (pH 7.0; 0.01 M) and acetonitrile (85:15, *v*/*v*). The flow rate was 0.9 mL/min, and the temperature was set to 25 °C. Detection of the tested compounds was performed at 230 and 280 nm. Retention factors were calculated using Equation (5), where t_0 (column dead time) was the retention time of DMSO at 220 nm.

$$k = (t_R - t_0)/t_0 \quad (5)$$

3.4. Protein–Ligand Interaction Modelling

3.4.1. Molecular Docking

The crystal structures of warfarin-bound HSA, ibuprofen-bound HSA, and myristic acid-bound HSA (PDB IDs: 2BXD, 2BXG, and 1BJ5, respectively), as well as LasR-OC12 HSL complex and AHL Synthase Lasl (PDB IDs: 3IX3 and 1RO5, respectively) were extracted from the RCSB Protein Data Bank (www.rcsb.org) [83]. The three-dimensional (3D) structures of monoanionic **TTNF37** and **1** were constructed using ChemBio3D Ultra 12.0 and optimized using the DMol3 module in Material Studio 2017, with the GGA PBE functional and DNP [84] approach. The hydrogen atoms of monoanionic **TTNF37**, (2-bromo-5-(2-bromo-2-nitrovinyl)furan (furvina G1), as well as all co-crystallized ligands, were normalized to standard values estimated by neutron diffraction. Preparation of each protein structure (protonation, removal of water molecules, setting of atom and bond types, as well as adjustment of the flexibility of amino acid side chains and residues building up the walls of canonical protein sites) was performed using the GOLD (Genetic Optimization for Ligand Docking) program implemented in the CSD-Enterprise Suite licensed version 2022.3.0 [85–88]. Calculations were performed to mimic physiological pH conditions, accurately representing the protonation states of amino acid side chains. The results are visually represented as 3D bioactive conformations within the main body of the paper. Furthermore, full 2D-schematic drawings of the interactions of the first GOLD cluster docked solutions for **TTNF37**, generated using LIGPLUS v.2.2. [69], are shown in the Supplementary (Figures S11 and S13). Ligand was docked to Sudlow sites 1 and 2 (domain IIA and IIIA, warfarin-bound-HSA and ibuprofen-bound-HSA, respectively) as well as in drug binding site 3 (domain IB in myristic acid-bound-HSA) in the generated cavity of a 10 Å radius. CHEMPLP was chosen as a fitness function, and the ligands were submitted to 50 genetic algorithm runs. Results differing by less than 1.0 Å in ligand all-atom RMSD were clustered together. The best GOLD-calculated conformation was used both for analysis and representation. The distribution of productive poses, as determined by cluster analysis of docking results using a 1.0 Å RMSD cluster tolerance, is provided in the Supplementary Material (Supplementary Figures S12 and S14). Ligand efficiency (LE) was calculated according to the formula for LE = Etot/N, where Etot is the estimated binding energy (in kcal mol^{-1}), and N is the number of heavy atoms in the ligand [11]. The number of heavy atoms for each compound was calculated from the molecular formula: **TTNF37** (18 atoms), **1** (17 atoms), warfarin (23 atoms), ibuprofen (15 atoms), myristic acid (16 atoms), 3-Oxo-C12-HSL (21 atoms), and furvina (G1) (12 atoms).

3.4.2. Molecular Dynamics Simulations

MD simulations of AHL synthase LasI and transcriptional activator LasR were performed using Desmond 2024-4 [89] with the OLPS-2005 force field [90] and Maestro 14.2.118 [91] as the graphical user interface. Docking-derived protein–ligand complexes were solvated in a cubic box of SPC water with a 15 Å buffer, neutralized with Na^+ ions, and adjusted to physiological ionic strength.

Systems were relaxed using Desmond's default protocol (restrained minimization and short MD runs). Electrostatics were treated with PME (9 Å cutoff), and SHAKE constrained bonds to hydrogens, enabling a 2 fs timestep. Temperature (300 K) was controlled by the Nose–Hoover thermostat (1 ps^{-1}), and pressure (1 bar) by the Martyna–Tobias–Klein barostat (1 ps relaxation). Production MD was run for 1 μs under NPT conditions, generating 1000 trajectory frames for protein and complexes. Subsequent analyses were performed in Maestro.

3.4.3. Statistical Analysis

Statistical analysis was performed using GraphPad Prism soft-ware version 8 (GraphPad Software Inc., San Diego, CA, USA). Significance was tested using one-way comparisons ANOVA and multiple comparisons based on ≥95% confidence level ($p < 0.05$, statistically significant). Statistical significance was defined as $p < 0.05$ (*), $p < 0.01$ (**), $p < 0.001$ (***), and $p < 0.0001$ (****). All experiments were conducted in duplicate with at least three replicates for each condition tested.

4. Conclusions

In this work, we tested the antimicrobial activity and anti-QS activity of novel PTH—**TTNF37** as well as its effects on biofilm formation and QS-regulated virulence factors. **TTNF37** is the first PTH that shows both good solubility and potent activity obtained by structural modification of HL, which also had good activity, but low solubility. **TTNF37** showed better antibacterial than antifungal activity. Of particular interest is the fact that the activity of this compound against *E. coli* is comparable to that of the control antibiotic. In addition, **TTNF37** interfered with the 3-oxo-C12-HSL-dependent QS system of *P. aeruginosa*, and its effect was dose-dependent, ranging from 26% to 98%. It is worth noting that the newly synthesised compound has a more pronounced effect on the detection than on the production of 3-oxo-C12-HSL, with a reduction in bioluminescence of about 65% being observed. Molecular docking studies supported by molecular dynamics confirmed the significant binding interactions, with binding values higher than those of furvina (a potent QS inhibitor studied by our research group) and similar to the natural autoinducer. In addition, **TTNF37** was able to inhibit pyocyanin production by 33% with only 25 μg/mL. The compound also reduced biofilm formation, promoting a decrease in biomass, metabolic activity, and culturability. Furthermore, **TTNF37** impaired the biofilm structure without compromising the membrane integrity of the adhered cells. Finally, the new hybrid was shown to interact strongly with the HSA protein and exist in anionic form at physiological pH. These results emphasise the potential of **TTNF37** as an effective compound with antimicrobial and anti-QS properties, making it a promising candidate for combating bacterial biofilm-related infections. Taking into account all previously mentioned results obtained for **TTNF37**, as well as the fact that it was practically inactive against the MRC-5 normal cell line, one can conclude that this compound is worth further investigation. In that respect, we plan to conduct a new study dealing with the development of suitable delivery systems for this compound, to overcome the difficulties that may be related to its strong ability to bind to HSA.

Supplementary Materials: The following supporting information can be downloaded at: https://www.mdpi.com/article/10.3390/ijms27041784/s1.

Author Contributions: A.B.: Conceptualization, Methodology, Validation, Investigation, Writing—review & editing, Project administration, Resources, Funding acquisition; S.K.: Methodology, Validation, Formal analysis, Investigation; M.M.L.: Investigation, Formal analysis, Writing—original draft; P.R.: Resources, Writing—review & editing; I.N.: Resources; V.D.: Resources; M.N.: Resources; M.Z.: Resources; T.R.T.: Resources, Writing—review & editing; M.S.: Resources, Funding acquisition, Writing—review & editing; N.R.F.: Project administration, Resources, Funding acquisition, Writing—review & editing. All authors have read and agreed to the published version of the manuscript.

Funding: This work was supported by: Project MultAntiBiofilm (ref. COMPETE2030-FEDER-00852000; Nº 17121); and HCAI_Disinfect (ref. COMPETE2030-FEDER-00752300; Nº 16360), funded through the Operational Programme Competitiveness Factors-COMPETE, and national funds by the Foundation for Science and Technology (FCT); Project InnovAntiBiofilm (ref. 101157363) financed by European Commission (Horizon-Widera 2023-Acess-02/Horizon-CSA); and LEPABE,

UIDB/00511/2020 (DOI: 10.54499/UIDB/00511/2020) and UIDP/00511/2020 (DOI: 10.54499/UIDP/00511/2020); ALiCE, LA/P/0045/2020 (DOI: 10.54499/LA/P/0045/2020), funded by national funds through the FCT/MCTES (PIDDAC; Lisbon, Portugal). Miguel M. Leitão (reference: 2021.07145.BD and DOI: https://doi.org/10.54499/2021.07145.BD) acknowledges individual PhD fellowships from FCT. This research was supported by the Ministry of Science, Technological Development and Innovation of the Republic of Serbia (Contract numbers: 451-03-136/2025-03/200168, 451-03-137/2025-03/200116, 451-03-136/2025-03/200161, and 451-03-137/2025-03/200161) and is in accordance with the 2030 Agenda for Sustainable Development of the United Nations (Goal 3: Good health and well-being; Goal 12: Responsible consumption and production; and Goal 17: Partnership for the goals). This article is also based upon work from COST Action EURESTOP, CA21145, supported by COST (European Cooperation in Science and Technology).

Institutional Review Board Statement: Not applicable.

Informed Consent Statement: Not applicable.

Data Availability Statement: The original contributions presented in this study are included in the article/Supplementary Material. Further inquiries can be directed to the corresponding authors.

Conflicts of Interest: The authors declare no conflicts of interest.

References

1. Haque, S.; Ahmad, F.; Dar, S.A.; Jawed, A.; Mandal, R.K.; Wahid, M.; Lohani, M.; Khan, S.; Singh, V.; Akhter, N. Developments in Strategies for Quorum Sensing Virulence Factor Inhibition to Combat Bacterial Drug Resistance. *Microb. Pathog.* **2018**, *121*, 293–302. [CrossRef] [PubMed]
2. Frieri, M.; Kumar, K.; Boutin, A. Antibiotic Resistance. *J. Infect. Public Health* **2017**, *10*, 369–378. [CrossRef]
3. Saxena, P.; Joshi, Y.; Rawat, K.; Bisht, R. Biofilms: Architecture, Resistance, Quorum Sensing and Control Mechanisms. *Indian J. Microbiol.* **2019**, *59*, 3–12. [CrossRef]
4. Gonçalves, A.S.C.; Leitão, M.M.; Simões, M.; Borges, A. The Action of Phytochemicals in Biofilm Control. *Nat. Prod. Rep.* **2023**, *40*, 595–627. [CrossRef] [PubMed]
5. Cendra Gascón, M.D.M.; Torrents Serra, E. *Pseudomonas aeruginosa* Biofilms and Their Partners in Crime. *Biotechnol. Adv.* **2021**, *49*, 107734. [CrossRef]
6. Diggle, S.P.; Crusz, S.A.; Cámara, M. Quorum Sensing. *Curr. Biol.* **2007**, *17*, 907–910. [CrossRef]
7. Moura-Alves, P.; Puyskens, A.; Stinn, A.; Klemm, M.; Guhlich-Bornhof, U.; Dorhoi, A.; Furkert, J.; Kreuchwig, A.; Protze, J.; Lozza, L.; et al. Host Monitoring of Quorum Sensing during *Pseudomonas aeruginosa* Infection. *Science* **2019**, *366*, eaaw1629. [CrossRef] [PubMed]
8. Smith, R.S.; Iglewski, B.H. *P. aeruginosa* Quorum-Sensing Systems and Virulence. *Curr. Opin. Microbiol.* **2003**, *6*, 56–60. [CrossRef]
9. Azimi, S.; Klementiev, A.D.; Whiteley, M.; Diggle, S.P. Bacterial Quorum Sensing during Infection. *Annu. Rev. Microbiol.* **2020**, *74*, 201–219. [CrossRef]
10. Leitão, M.M.; Vieira, T.F.; Sousa, S.F.; Borges, F.; Simões, M.; Borges, A. Dual Action of Benzaldehydes: Inhibiting Quorum Sensing and Enhancing Antibiotic Efficacy for Controlling *Pseudomonas aeruginosa* Biofilms. *Microb. Pathog.* **2024**, *191*, 106663. [CrossRef]
11. Borges, A.; Simões, M.; Todorović, T.R.; Filipović, N.R.; Garcia-Sosa, A.T. Cobalt Complex with Thiazole-Based Ligand as New *Pseudomonas aeruginosa* Quorum Quencher, Biofilm Inhibitor and Virulence Attenuator. *Molecules* **2018**, *23*, 1385. [CrossRef]
12. Pesci, E.C.; Pearson, J.P.; Seed, P.C.; Iglewski, B.H. Regulation of Las and Rhl Quorum Sensing in *Pseudomonas aeruginosa*. *J. Bacteriol.* **1997**, *179*, 3127–3132. [CrossRef]
13. Xiao, G.; He, J.; Rahme, L.G. Mutation Analysis of the *Pseudomonas aeruginosa* MvfR and PqsABCDE Gene Promoters Demonstrates Complex Quorum-Sensing Circuitry. *Microbiology* **2006**, *152*, 1679–1686. [CrossRef]
14. Kalia, V.C.; Patel, S.K.S.; Kang, Y.C.; Lee, J.K. Quorum Sensing Inhibitors as Antipathogens: Biotechnological Applications. *Biotechnol. Adv.* **2019**, *37*, 68–90. [CrossRef] [PubMed]
15. Borges, A.; Sousa, P.; Gaspar, A.; Vilar, S.; Borges, F.; Simões, M. Furvina Inhibits the 3-Oxo-C12-HSL-Based Quorum Sensing System of *Pseudomonas aeruginosa* and QS-Dependent Phenotypes. *Biofouling* **2017**, *33*, 156–168. [CrossRef]
16. Singh, L.R.; Avula, S.R.; Raj, S.; Srivastava, A.; Palnati, G.R.; Tripathi, C.K.M.; Pasupuleti, M.; Sashidhara, K.V. Coumarin-Benzimidazole Hybrids as a Potent Antimicrobial Agent: Synthesis and Biological Elevation. *J. Antibiot.* **2017**, *70*, 954–961. [CrossRef] [PubMed]
17. Gao, F.; Xiao, J.; Huang, G. Current Scenario of Tetrazole Hybrids for Antibacterial Activity. *Eur. J. Med. Chem.* **2019**, *184*, 111744. [CrossRef] [PubMed]

18. Domalaon, R.; Idowu, I.; Zhanel, G.G.; Schweizer, F. Antibiotic Hybrids: The Next Generation of Agents And Adjuvants against Gram-Negative Pathogens? *Clin. Microbiol. Rev.* **2018**, *31*, e00077-17. [CrossRef]
19. Amariucai-Mantu, D.; Mangalagiu, V.; Bejan, I.; Aricu, A.; Mangalagiu, I.I. Hybrid Azine Derivatives: A Useful Approach for Antimicrobial Therapy. *Pharmaceutics* **2022**, *14*, 2026. [CrossRef]
20. Lungu, I.A.; Moldovan, O.L.; Biriș, V.; Rusu, A. Fluoroquinolones Hybrid Molecules as Promising Antibacterial Agents in the Fight against Antibacterial Resistance. *Pharmaceutics* **2022**, *14*, 1749. [CrossRef]
21. Marshall, C.M.; Federice, J.G.; Bell, C.N.; Cox, P.B.; Njardarson, J.T. An Update on the Nitrogen Heterocycle Compositions and Properties of U.S. FDA-Approved Pharmaceuticals (2013–2023). *J. Med. Chem.* **2024**, *67*, 11622–11655. [CrossRef]
22. De, S.; S K, A.K.; Shah, S.K.; Kazi, S.; Sarkar, N.; Banerjee, S.; Dey, S. Pyridine: The Scaffolds with Significant Clinical Diversity. *RSC Adv.* **2022**, *12*, 15385–15406. [CrossRef]
23. Ling, Y.; Hao, Z.Y.; Liang, D.; Zhang, C.L.; Liu, Y.F.; Wang, Y. The Expanding Role of Pyridine and Dihydropyridine Scaffolds in Drug Design. *Drug Des. Devel. Ther.* **2021**, *15*, 4289–4338. [CrossRef] [PubMed]
24. Wishart, D.S.; Knox, C.; Guo, A.C.; Shrivastava, S.; Hassanali, M.; Stothard, P.; Chang, Z.; Woolsey, J. Drugbank: A Comprehensive Resource for in Silico Drug Discovery and Exploration. *Nucleic Acids Res.* **2006**, *34*, 668–672. [CrossRef] [PubMed]
25. U.S. Dept. of Health and Human Services, Food and Drug Administration, Center for Drug Evaluation and Research, Office of Pharmaceutical Science, Office of Generic Drugs. *Approved Drug Products*, 42nd ed.; U.S. Dept. of Health and Human Services, Food and Drug Administration, Center for Drug Evaluation and Research, Office of Pharmaceutical Science, Office of Generic Drugs: Silver Spring, MD, USA, 2022.
26. Khamitova, A.; Berillo, D.; Lozynskyi, A.; Konechnyi, Y.; Mural, D.; Georgiyants, V.; Lesyk, R. Thiadiazole and Thiazole Derivatives as Potential Antimicrobial Agents. *Mini Rev. Med. Chem.* **2024**, *24*, 531–545. [CrossRef] [PubMed]
27. Dyniewicz, J.; Lipinski, P.F.J.; Kosson, P.; Lesniak, A.; Bochynska-Czyz, M.; Muchowska, A.; Tourwe, D.; Ballet, S.; Misicka, A.; Lipkowski, A.W. Hydrazone Linker as a Useful Tool for Preparing Chimeric Peptide/Nonpeptide Bifunctional Compounds. *ACS Med. Chem. Lett.* **2017**, *8*, 73–77. [CrossRef]
28. Araškov, J.B.; Srdić-Rajić, T.; Višnjevac, A.; Blagojević, V.; Todorović, T.R.; Filipović, N.R. Mononuclear Isothiocyanate Zinc Complex with a Pyridine-Based Thiazolyl-Hydrazone Ligand: Transformation into a 1D Coordination Polymer and Anticancer Activity against Pancreatic Cancer Cell Lines. *Inorg. Chem. Commun.* **2025**, *182*, 115651. [CrossRef]
29. Filipović, N.R.; Elshaflu, H.; Grubišić, S.; Jovanović, L.S.; Rodić, M.; Novaković, I.; Malešević, A.; Djordjević, I.S.; Li, H.; Šojić, N.; et al. Co(III) Complexes of (1,3-Selenazol-2-yl)Hydrazones and Their Sulphur Analogues. *Dalt. Trans.* **2017**, *46*, 2910–2924. [CrossRef]
30. Kokanov, S.; Nikolić, M.; Novaković, I.; Todorović, T.; Filipović, N. Synthesis, Characterization, and Evaluation of Antioxidant and Antimicrobial Activity of Three Novel *N*-Heteroaromatic Hydrazonyl-Thiazoles. *Adv. Technol.* **2021**, *10*, 14–23. [CrossRef]
31. Rehman, M.T.; Khan, A.U. Understanding the Interaction between Human Serum Albumin and Anti-Bacterial/Anti-Cancer Compounds. *Curr. Pharm. Des. Des.* **2015**, *21*, 1785–1799. [CrossRef]
32. Nakamoto, K. *Infrared and Raman Spectra of Inorganic and Coordination Compounds: Part A: Theory and Applications in Inorganic Chemistry*, 6th ed.; John Wiley & Sons: Hoboken, NJ, USA, 2008.
33. Kokanov, S.B.; Filipović, N.R.; Višnjevac, A.; Nikolić, M.; Novaković, I.; Janjić, G.; Holló, B.B.; Ramotowska, S.; Nowicka, P.; Makowski, M.; et al. A Detailed Experimental and Computational Study of Cd Complexes with Pyridyl-based Thiazolyl Hydrazones. *Appl. Organomet. Chem.* **2022**, *37*, e6942. [CrossRef]
34. Kowol, C.R.; Miklos, W.; Pfaff, S.; Hager, S.; Kallus, S.; Pelivan, K.; Kubanik, M.; Enyedy, É.A.; Berger, W.; Heffeter, P.; et al. Impact of Stepwise NH_2-Methylation of Triapine on the Physicochemical Properties, Anticancer Activity, and Resistance Circumvention. *J. Med. Chem.* **2016**, *59*, 6739–6752. [CrossRef]
35. Filipović, N.; Todorović, T.; Marković, R.; Marinković, A.; Tufegdžić, S.T.; Godevac, D.; Andelković, K. Synthesis, Characterization and Biological Activities of N-Heteroaromatic Hydrazones and Their Complexes with Pd(II), Pt(II) and Cd(II). *Transit. Met. Chem.* **2010**, *35*, 765–772. [CrossRef]
36. Rossi, S.A.; De Oliveira, H.C.; Agreda-Mellon, D.; Lucio, J.; Soares Mendes-Giannini, M.J.; García-Cambero, J.P.; Zaragoza, O. Identification of Off-Patent Drugs That Show Synergism with Amphotericin B or That Present Antifungal Action against *Cryptococcus neoformans* and *Candida* spp. *Antimicrob. Agents Chemother.* **2020**, *64*, e01921-19. [CrossRef] [PubMed]
37. Kassab, R.M.; Al-Hussain, S.A.; Elleboudy, N.S.; Albohy, A.; Zaki, M.E.A.; Abouzid, K.A.M.; Muhammad, Z.A. Tackling Microbial Resistance with Isatin-Decorated Thiazole Derivatives: Design, Synthesis, and in Vitro Evaluation of Antimicrobial and Antibiofilm Activity. *Drug Des. Devel. Ther.* **2022**, *16*, 2817–2832. [CrossRef]
38. Roy, P.K.; Song, M.G.; Park, S.Y. The Inhibitory Effect of Quercetin on Biofilm Formation of Listeria Monocytogenes Mixed Culture and Repression of Virulence. *Antioxidants* **2022**, *11*, 1733. [CrossRef] [PubMed]
39. Ecevit, K.; Barros, A.A.; Silva, J.M.; Reis, R.L. Preventing Microbial Infections with Natural Phenolic Compounds. *Future Pharmacol.* **2022**, *2*, 460–498. [CrossRef]

40. Ong, K.S.; Mawang, C.I.; Daniel-Jambun, D.; Lim, Y.Y.; Lee, S.M. Current Anti-Biofilm Strategies and Potential of Antioxidants in Biofilm Control. *Expert Rev. Anti. Infect. Ther.* **2018**, *16*, 855–864. [CrossRef] [PubMed]
41. Wei, Q.; Le Minh, P.N.; Dötsch, A.; Hildebrand, F.; Panmanee, W.; Elfarash, A.; Schulz, S.; Plaisance, S.; Charlier, D.; Hassett, D.; et al. Global Regulation of Gene Expression by OxyR in an Important Human Opportunistic Pathogen. *Nucleic Acids Res.* **2012**, *40*, 4320–4333. [CrossRef]
42. Njus, D.; Kelley, P.M.; Tu, Y.J.; Schlegel, H.B. Ascorbic Acid: The Chemistry Underlying Its Antioxidant Properties. *Free Radic. Biol. Med.* **2020**, *159*, 37–43. [CrossRef]
43. Boulebd, H.; Zine, Y.; Khodja, I.A.; Mermer, A.; Demir, A.; Debache, A. Synthesis and Radical Scavenging Activity of New Phenolic Hydrazone/Hydrazide Derivatives: Experimental and Theoretical Studies. *J. Mol. Struct.* **2022**, *1249*, 131546. [CrossRef]
44. Kareem, H.S.; Ariffin, A.; Nordin, N.; Heidelberg, T.; Abdul-Aziz, A.; Kong, K.W.; Yehye, W.A. Correlation of Antioxidant Activities with Theoretical Studies for New Hydrazone Compounds Bearing a 3,4,5-Trimethoxy Benzyl Moiety. *Eur. J. Med. Chem.* **2015**, *103*, 497–505. [CrossRef]
45. Jaishree, V.; Ramdas, N.; Sachin, J.; Ramesh, B. In Vitro Antioxidant Properties of New Thiazole Derivatives. *J. Saudi Chem. Soc.* **2012**, *16*, 371–376. [CrossRef]
46. Kaddouri, Y.; Abrigach, F.; Yousfi, E.B.; El Kodadi, M.; Touzani, R. New Thiazole, Pyridine and Pyrazole Derivatives as Antioxidant Candidates: Synthesis, DFT Calculations and Molecular Docking Study. *Heliyon* **2020**, *6*, e03185. [CrossRef] [PubMed]
47. Araškov, J.B.; Nikolić, M.; Armaković, S.; Armaković, S.; Rodić, M.; Višnjevac, A.; Padrón, J.M.; Todorović, T.R.; Filipović, N.R. Structural, Antioxidant, Antiproliferative and In–silico Study of Pyridine-Based Hydrazonyl–Selenazoles and Their Sulphur Isosteres. *J. Mol. Struct.* **2021**, *1240*, 130512. [CrossRef]
48. Abdelsamie, A.S.; Hamed, M.M.; Schütz, C.; Röhrig, T.; Kany, A.M.; Schmelz, S.; Blankenfeldt, W.; Hirsch, A.K.H.; Hartmann, R.W.; Empting, M. Discovery and Optimization of Thiazole-Based Quorum Sensing Inhibitors as Potent Blockers of *Pseudomonas aeruginosa* Pathogenicity. *Eur. J. Med. Chem.* **2024**, *276*, 116685. [CrossRef]
49. Talaat, R.; Abu El-Naga, M.N.; El-Bialy, H.A.A.; El-Fouly, M.Z.; Abouzeid, M.A. Quenching of Quorum Sensing in Multi-Drug Resistant *Pseudomonas aeruginosa*: Insights on Halo-Bacterial Metabolites and Gamma Irradiation as Channels Inhibitors. *Ann. Clin. Microbiol. Antimicrob.* **2024**, *23*, 31. [CrossRef] [PubMed]
50. Lidor, O.; Al-Quntar, A.; Pesci, E.C.; Steinberg, D. Mechanistic Analysis of a Synthetic Inhibitor of the *Pseudomonas aeruginosa* LasI Quorum-Sensing Signal Synthase. *Sci. Rep.* **2015**, *5*, 16569, Erratum in *Sci. Rep.* **2016**, *6*, 25257. [CrossRef]
51. Ammar, Y.A.; Ragab, A.; Migahed, M.A.; Al-Sharbasy, S.; Salem, M.A.; Riad, O.K.M.; Selim, H.M.R.M.; Abd-Elmaksoud, G.A.; Abusaif, M.S. Design, Green Synthesis, and Quorum Sensing Quenching Potential of Novel 2-Oxo-Pyridines Containing a Thiophene/Furan Scaffold and Targeting a LasR Gene on *P. aeruginosa*. *RSC Adv.* **2023**, *13*, 27363–27384. [CrossRef]
52. Mudaliar, S.B.; Bharath Prasad, A.S. A Biomedical Perspective of Pyocyanin from *Pseudomonas aeruginosa*: Its Applications and Challenges. *World J. Microbiol. Biotechnol.* **2024**, *40*, 90. [CrossRef]
53. Sultan, M.; Arya, R.; Kim, K.K. Roles of Two-Component Systems in *Pseudomonas aeruginosa* Virulence. *Int. J. Mol. Sci.* **2021**, *22*, 12152. [CrossRef]
54. Leitão, M.M.; Gonçalves, A.S.C.; Moreira, J.; Fernandes, C.; Borges, F.; Simões, M.; Borges, A. Unravelling the Potential of Natural Chelating Agents in the Control of *Staphylococcus aureus* and *Pseudomonas aeruginosa* Biofilms. *Eur. J. Med. Chem.* **2025**, *283*, 117163. [CrossRef]
55. Braud, A.; Geoffroy, V.; Hoegy, F.; Mislin, G.L.A.; Schalk, I.J. Presence of the Siderophores Pyoverdine and Pyochelin in the Extracellular Medium Reduces Toxic Metal Accumulation in *Pseudomonas aeruginosa* and Increases Bacterial Metal Toleranceemi. *Environ. Microbiol. Rep.* **2010**, *2*, 419–425. [CrossRef]
56. Li, S.; Chen, S.; Fan, J.; Cao, Z.; Ouyang, W.; Tong, N.; Hu, X.; Hu, J.; Li, P.; Feng, Z.; et al. Anti-Biofilm Effect of Novel Thiazole Acid Analogs against *Pseudomonas aeruginosa* through IQS Pathways. *Eur. J. Med. Chem.* **2018**, *145*, 64–73. [CrossRef]
57. Simões, M.; Bennett, R.N.; Rosa, E.A.S. Understanding Antimicrobial Activities of Phytochemicals against Multidrug Resistant Bacteria and Biofilms. *Nat. Prod. Rep.* **2009**, *26*, 746–757. [CrossRef]
58. Borges, A.; Abreu, A.C.; Dias, C.; Saavedra, M.J.; Borges, F.; Simões, M. New Perspectives on the Use of Phytochemicals as an Emergent Strategy to Control Bacterial Infections Including Biofilms. *Molecules* **2016**, *21*, 877. [CrossRef]
59. da Costa Lima, J.L.; Alves, L.R.; de Araújo Jacomé, P.R.L.; Bezerra Neto, J.P.; Maciel, M.A.V.; de Morais, M.M.C. Biofilm Production by Clinical Isolates of *Pseudomonas aeruginosa* and Structural Changes in LasR Protein of Isolates Non Biofilm-Producing. *Braz. J. Infect. Dis.* **2018**, *22*, 129–136. [CrossRef]
60. Hemmati, J.; Nazari, M.; Abolhasani, F.S.; Ahmadi, A.; Asghari, B. In Vitro Investigation of Relationship between Quorum-Sensing System Genes, Biofilm Forming Ability, and Drug Resistance in Clinical Isolates of *Pseudomonas aeruginosa*. *BMC Microbiol.* **2024**, *24*, 99. [CrossRef] [PubMed]
61. Mohammed, E.Z.; El-Dydamony, N.M.; Taha, E.A.; Taha, M.N.; Mehany, A.B.M.; Abdel Aziz, H.A.; Abd El-Aleam, R.H. Design, Synthesis, and Molecular Dynamic Simulations of Some Novel Benzo[d]Thiazoles with Anti-Virulence Activity Against *Pseudomonas aeruginosa*. *Eur. J. Med. Chem.* **2024**, *279*, 116880. [CrossRef] [PubMed]

62. Lejon, S.; Cramer, J.F.; Nordberg, P. Structural Basis for the Binding of Naproxen to Human Serum Albumin in the Presence of Fatty Acids and the GA Module. *Acta Crystallogr. Sect. F Struct. Biol. Cryst. Commun.* **2008**, *64*, 64–69. [CrossRef] [PubMed]
63. Aarons, L.; Khan, A.Z.; Grennan, D.M.; Alam-Siddiqi, M. The Binding of Flurbiprofen to Plasma Proteins. *J. Pharm. Pharmacol.* **1985**, *37*, 644–646. [CrossRef]
64. Milligan, T.P.; Morris, H.C.; Hammond, P.M.; Price, C.P. Studies on Paracetamol Binding to Serum Proteins. *Ann. Clin. Biochem.* **1994**, *31*, 492–496. [CrossRef]
65. Wu, L.; Luo, Y. Bacterial Quorum-Sensing Systems and Their Role in Intestinal Bacteria-Host Crosstalk. *Front. Microbiol.* **2021**, *12*, 611413. [CrossRef] [PubMed]
66. Steindler, L.; Bertani, I.; De Sordi, L.; Schwager, S.; Eberl, L.; Venturi, V. LasI/R and RhlI/R Quorum Sensing in a Strain of *Pseudomonas aeruginosa* Beneficial to Plants. *Appl. Environ. Microbiol.* **2009**, *75*, 5131–5140. [CrossRef]
67. *Marvin*, Version 21.17.0; ChemAxon: Budapest, Hungary, 2021. Available online: https://www.chemaxon.com (accessed on 6 February 2023).
68. Fanali, G.; Di Masi, A.; Trezza, V.; Marino, M.; Fasano, M.; Ascenzi, P. Human Serum Albumin: From Bench to Bedside. *Mol. Aspects Med.* **2012**, *33*, 209–290. [CrossRef] [PubMed]
69. Laskowski, R.A.; Swindells, M.B. LigPlot+: Multiple Ligand–Protein Interaction Diagrams for Drug Discovery. *J. Chem. Inf. Model.* **2011**, *51*, 2778–2786. [CrossRef] [PubMed]
70. Zelenović, N.D.; Ristić, P.; Polović, N.D.; Todorović, T.R.; Kojadinović, M.; Popović, M. A Multi-Spectroscopic and Molecular Docking Analysis of the Biophysical Interaction between Food Polyphenols, Urolithins, and Human Serum Albumin. *Molecules* **2024**, *29*, 4474. [CrossRef]
71. *CLSI M07-Ed11*; Methods for Dilution Antimicrobial Susceptibility Tests That Grow Aerobically-11th Edition. Clinical and Laboratory Standards Institute: Wayne, PA, USA, 2018.
72. Dagmar, B.; Stengel, S.C. (Eds.) *Natural Products From Marine Algae: Methods and Protocols*; Springer Science+Business Media: New York, NY, USA, 2015.
73. Elshaflu, H.; Todorović, T.R.; Nikolić, M.; Lolić, A.; Višnjevac, A.; Hagenow, S.; Padrón, J.M.; García-Sosa, A.T.; Djordjevic, I.S.; Grubišic, S.; et al. Selenazolyl-Hydrazones as Novel Selective MAO Inhibitors with Antiproliferative and Antioxidant Activities: Experimental and In-Silico Studies. *Front. Chem.* **2018**, *6*, 247. [CrossRef]
74. Massai, F.; Imperi, F.; Quattrucci, S.; Zennaro, E.; Visca, P.; Leoni, L. A Multitask Biosensor for Micro-Volumetric Detection of N-3-Oxo-Dodecanoyl-Homoserine Lactone Quorum Sensing Signal. *Biosens. Bioelectron.* **2011**, *26*, 3444–3449. [CrossRef]
75. Essar, D.W.; Eberly, L.; Hadero, A.; Crawford, I.P. Identification and Characterization of Genes for a Second Anthranilate Synthase in *Pseudomonas aeruginosa*: Interchangeability of the Two Anthranilate Synthase and Evolutionary Implications. *J. Bacteriol.* **1990**, *172*, 884–900. [CrossRef]
76. Höfte, M.; Buysens, S.; Koedam, N.; Cornelis, P. Zinc Affects Siderophore-Mediated High Affinity Iron Uptake Systems in the Rhizosphere *Pseudomonas aeruginosa* 7NSK2. *Biometals* **1993**, *6*, 85–91. [CrossRef]
77. Yang, L.; Rybtke, M.T.; Jakobsen, T.H.; Hentzer, M.; Bjarnsholt, T.; Givskov, M.; Tolker-Nielsen, T. Computer-Aided Identification of Recognized Drugs as *Pseudomonas aeruginosa* Quorum-Sensing Inhibitors. *Antimicrob. Agents Chemother.* **2009**, *53*, 2432–2443. [CrossRef]
78. Leitão, M.M.; Gonçalves, A.S.C.; Sousa, S.F.; Borges, F.; Simões, M.; Borges, A. Two Cinnamic Acid Derivatives as Inhibitors of *Pseudomonas aeruginosa* Las and Pqs Quorum-Sensing Systems: Impact on Biofilm Formation and Virulence Factors. *Biomed. Pharmacother.* **2025**, *187*, 118090. [CrossRef]
79. Borges, A.; Simoes, L.C.; Saavedra, M.J.; Simoes, M. The Action of Selected Isothiocyanates on Bacterial Biofilm Prevention and Control. *Int. Biodeterior. Biodegrad.* **2014**, *86*, 25–33. [CrossRef]
80. Vieira, T.F.; Leitão, M.M.; Cerqueira, N.M.F.S.A.; Sousa, S.F.; Borges, A.; Simões, M. Montelukast and Cefoperazone Act as Antiquorum Sensing and Antibiofilm Agents against *Pseudomonas aeruginosa*. *J. Appl. Microbiol.* **2024**, *135*, lxae088. [CrossRef]
81. Narciso, D.A.; Pereira, A.; Dias, N.O.; Melo, L.F.; Martins, F.G. Characterization of Biofilm Structure and Properties via Processing of 2D Optical Coherence Tomography Images in BISCAP. *Bioinformatics* **2022**, *38*, 1708–1715. [CrossRef] [PubMed]
82. Bošković, J.; Dobričić, V.; Savić, J.; Rupar, J.; Aleksić, M.; Marković, B.; Čudina, O. In Vitro Evaluation of Pharmacokinetic Properties of Selected Dual COX-2 and 5-LOX Inhibitors. *Pharmaceuticals* **2024**, *17*, 1329. [CrossRef] [PubMed]
83. Berman, H.; Henrick, K.; Nakamura, H. Announcing the Worldwide Protein Data Bank. *Nat. Struct. Biol.* **2003**, *10*, 980. [CrossRef]
84. *BIOVIA Material Studio*, Version 2017; Dassault Systèmes: San Diego, CA, USA, 2016.
85. Verdonk, M.L.; Cole, J.C.; Hartshorn, M.J.; Murray, C.W.; Taylor, R.D. Improved Protein–Ligand Docking Using GOLD Marcel. *Proteins Struct. Funct. Bioinform.* **2003**, *52*, 609–623. [CrossRef] [PubMed]
86. Jones, G.; Willett, P.; Glen, R.C. Molecular Recognition of Receptor Sites Using a Genetic Algorithm with a Description of Desolvation. *J. Mol. Biol.* **1995**, *245*, 43–53. [CrossRef]
87. Nissink, J.W.M.; Murray, C.; Hartshorn, M.; Verdonk, M.L.; Cole, J.C.; Taylor, R. A New Test Set for Validating Predictions of Protein–Ligand Interaction. *Proteins Struct. Funct. Bioinform.* **2002**, *49*, 457–471. [CrossRef] [PubMed]

88. Hartshorn, M.J.; Verdonk, M.L.; Chessari, G.; Brewerton, S.C.; Mooij, W.T.M.; Mortenson, P.N.; Murray, C.W. Diverse, High-Quality Test Set for the Validation of Protein−Ligand Docking Performance. *J. Med. Chem.* **2007**, *50*, 726–741. [CrossRef] [PubMed]
89. *Desmond Molecular Dynamics System*, 2024-4; D.E. Shaw Research: New York, NY, USA, 2024.
90. Banks, J.L.; Beard, H.S.; Cao, Y.; Cho, A.E.; Damm, W.; Farid, R.; Felts, A.K.; Halgren, T.A.; Mainz, D.T.; Maple, J.R.; et al. Integrated Modeling Program, Applied Chemical Theory (IMPACT). *J. Comutational. Chem.* **2005**, *26*, 1752–1780. [CrossRef] [PubMed]
91. *Maestro*, Version 14.2.118; Schrödinger, LLC: New York, NY, USA, 2024.

Disclaimer/Publisher's Note: The statements, opinions and data contained in all publications are solely those of the individual author(s) and contributor(s) and not of MDPI and/or the editor(s). MDPI and/or the editor(s) disclaim responsibility for any injury to people or property resulting from any ideas, methods, instructions or products referred to in the content.